Shallow fault zone structure affects rupture dynamics and ground motions of the 2019 Ridgecrest sequence to regional distances

Nico Schliwa[1], Alice-Agnes Gabriel[2,1], Yehuda Ben-Zion[3]

[1]Department of Earth and Environmental Sciences, Ludwig-Maximilians Universität München, Munich, Germany

[2]Scripps Institution of Oceanography, UC San Diego, La Jolla, USA

[3]Department of Earth Sciences and Statewide California Earthquake Center, University of Southern California, Los Angeles, USA

This is a non-peer-reviewed preprint submitted to EarthArXiv.

Key Points:

- Dynamic rupture simulations of the 2019 Ridgecrest foreshock and mainshock with a flower-shaped fault damage zone structure are presented.
- This fault zone affects ground motions at distances >100 km, with frequency-dependent effects related to its eigenfrequencies.
- Fault zone-induced supershear transitions may be less common than predicted by previous studies assuming constant friction parameters.

Corresponding author: Nico Schliwa, `nico.schliwa@lmu.de`

Abstract

Seismic faults are surrounded by damaged rocks with reduced rigidity and enhanced attenuation. These damaged fault zone structures can amplify seismic waves and affect earthquake dynamics, yet they are typically omitted in physics-based regional ground motion simulations. We report on the significant effects of a shallow, flower-shaped fault zone in foreshock-mainshock 3D dynamic rupture models of the 2019 Ridgecrest earthquake sequence. We find that the fault zone structure both amplifies and reduces ground motions not only locally but at distances exceeding 100 km. This impact on ground motions is frequency- and magnitude-dependent, particularly affecting higher frequency ground motions from the foreshock because its corner frequency is closer to the fault zone's fundamental eigenfrequency. Within the fault zone, the shallow transition to a velocity-strengthening frictional regime leads to a depth-dependent peak slip rate increase of up to 70% and confines fault zone-induced supershear transitions mostly to the fault zone's velocity-weakening bottom half. However, the interplay of fault zone waves, free surface reflections, and rupture directivity can generate localized supershear rupture, even in narrow velocity-strengthening regions, which are typically thought to inhibit supershear rupture. This study demonstrates that shallow fault zone structures may significantly affect intermediate- and far-field ground motions and cause localized supershear rupture penetrating into velocity-strengthening regions, with important implications for seismic hazard assessment.

Plain Language Summary

Earthquake-hosting geological faults in the Earth's crust are usually surrounded by damaged rock with reduced seismic wave propagation speeds. Sharp velocity contrasts within the damaged rock lead to reflections and trapping of seismic waves. These waves induce stress perturbations back on the fracture surface and interact nonlinearly with the earthquake's rupture process. We simulate the impact of shallow damaged rocks surrounding the rupture planes in a complex computer model of the 2019 Rigecrest sequence, including an M_w 6.4 foreshock and the M_w 7.1 mainshock. Rupture modifications and the distortion of the wavefield leaving the fault zone affect ground motions over large distances ($>$ 100 km) and cause an irregular pattern of amplification and deamplification. The impact on ground motions is stronger for frequencies above $\sim$ 0.5 Hz corresponding to the fundamental standing wave between the damaged rock's sharp velocity contrasts. The amplified fault zone waves can cause a transition to supersonic rupture speeds.

However, integrating realistic depth-dependent frictional properties suppresses high rupture velocities, leading to only locally confined supersonic rupture speeds. This study reveals the strong impact of shallow damaged rock on earthquake rupture and ground motions beyond the source region, affecting seismic hazard assessment on regional scales.

1 Introduction

The velocity structure around large fault zones can significantly alter the local seismic wavefield (Cormier & Spudich, 1984; Ben-Zion et al., 2003; Kurzon et al., 2014; Catchings et al., 2020) and earthquake rupture properties (e.g., Ben-Zion & Huang, 2002; Sammis et al., 2009; Huang et al., 2014; Xu et al., 2015). For example, sharp bimaterial interfaces generate head waves that can interact with dynamic ruptures and distort derived earthquake source properties (e.g., Ben-Zion, 1990; Andrews & Ben-Zion, 1997; Allam et al., 2014). Coherent low-velocity zones generate trapped waves and resonance modes that amplify local ground motions (e.g., Li & Leary, 1990; Igel et al., 2002; Hillers et al., 2014; Qiu et al., 2020). Numerical studies have shown that fault zone waves can cause pulse-like ruptures, rupture arrest, variations in rupture speed and off-fault damage, sustained transition to supershear, and back-propagating rupture fronts (Huang & Ampuero, 2011; Huang et al., 2014, 2016; Pelties et al., 2015; Flores-Cuba et al., 2024). However, many of these studies rely on simplified fault geometries and 2D frameworks and often lack direct observational constraints.

The extent to which fault zone structures can affect the behavior of earthquakes and generated ground motions is a subject of continuing research (Thakur et al., 2020; Abdelmeguid & Elbanna, 2022; Flores-Cuba et al., 2024). Further progress requires accounting for more realistic source models (e.g., Ulrich et al., 2019; Taufiqurrahman, Gabriel, Ulrich, et al., 2022) and 3D material properties (e.g., Rodgers et al., 2020; Z. Hu et al., 2022). Yeh and Olsen (2023) modeled the seismic radiation from the 2019 Ridgecrest earthquake using a kinematic source model (Liu et al., 2019) and a data-constrained local velocity model that included low-velocity fault zone structures (Zhou et al., 2022). Their results show that the fault zone structure considerably affects ground motions near the source and into the Los Angeles basin by generating Love waves at its boundaries. Regional-scale dynamic rupture simulations are computationally challenging but are now feasible with advances in high-performance computing (Uphoff et al., 2017; Folch et al., 2023). Dynamic source models can ensure physical consistency while simultaneously capturing the impact of a fault zone on the wavefield and the rupture process under lab-constrained friction conditions (Kaneko et al., 2008; Dunham et al., 2011).

Here, we integrate a complex flower-shaped fault zone (see Sec. 2.3, Qiu et al., 2021) into linked foreshock-mainshock regional dynamic rupture models of the 2019 Ridgcrest sequence (Sec. 2.1, Taufiqurrahman et al., 2023), including the M_w 6.4 Searles Valley foreshock and the M_w 7.1 Ridgecrest mainshock in the Eastern California Shear Zone (Ross et al., 2019; Goldberg et al., 2020; Chen et al., 2020). The model is embedded in a 3D velocity structure (Lee et al., 2014), incorporates a complex 3D quasi-orthogonal fault geometry, and fits a wide range of observations. Our results illustrate how the fault zone controls key rupture properties and modifies the seismic wavefield on both local and regional scales. The coupling of fault zone structures with simulated ground motions highlights the need to incorporate detailed local velocity models into ground motion simulations for large-scale earthquake scenarios.

2 Methods

2.1 3D dynamic rupture model setup of the 2019 Ridgecrest sequence

We compare two linked foreshock-mainshock dynamic rupture scenarios of the 2019 Ridgecrest sequence, without and with a fault damage zone: a "reference" model, which is based on previous work of Taufiqurrahman et al. (2023), and a "fault zone" (FZ) model, which adds a low-velocity damage zone around all rupture planes of the reference model (Sec. 2.3 and Fig. 1a). The dynamic rupture simulations are performed using the open-source software SeisSol (Text S1).

Taufiqurrahman et al. (2023) show that the dynamic and static mainshock-foreshock interactions during the Ridgecrest sequence can be explained by assuming overpressurized fluids and statically strong but dynamically weak faults. They used a wide range of geophysical data sets and incorporated multiple earthquake physics-relevant processes to construct the reference model. In the following, we briefly summarize the reference model setup and describe the reference model's rupture dynamics (Fig. S1).

To establish the initial 3D stress state, long-term Coulomb failure stress changes from previous large regional earthquakes (Verdecchia & Carena, 2016) are added to a tectonic background model (Yang & Hauksson, 2013). The mainshock model accounts for the stress changes induced by the foreshock model. Geologic field mapping, InSAR data, relocated seismicity, and selected focal mechanisms (Carena & Suppe, 2002) are combined to construct a quasi-orthogonal 3D fault system (Fig. 1b,c). A fast velocity-weakening rate-and-state friction law (Dunham et al., 2011) governs coseismic slip evolution (Table S1, Fig. S2). The dynamic rupture simulation incorporates off-fault plastic deformation and viscoelastic attenuation, linked to the 3D velocity structure via $Q_s = 0.1 v_s$ and $Q_p = 1.5\, Q_s$ (Olsen et al., 2003). The model domain's material properties represent a 3D velocity model of southern California (CVM-S4.26; Lee et al., 2014; Small et al., 2017) and it includes high-resolution topography (Farr et al., 2007). The simulations allow resolving seismic wave propagation up to at least 2 Hz in the near-source region and up to at least 1 Hz in the full study region, which expands to distances up to 140 km away from the Ridgecrest fault system (Text S2).

2.2 Reference model rupture dynamics

The complex rupture dynamics of the foreshock and mainshock in the reference model (Fig. S1) explain a broad set of strong-motion, teleseismic, field mapping, GNSS, and InSAR observations. The Searles Valley foreshock scenario is nucleated near the intersection of F1 and F2 at a depth of 10.5 km. Rupture on F1 halts soon after initiation, not reaching the surface due to non-optimal fault orientation, while rupture on F2 reaches the surface and continues to its southwestern end (Fig. 1). In the reference mainshock model, rupture initially propagates as a bilateral crack across the northern part of F3 after forced nucleation at a depth of 8 km. The rupture arrests smoothly to the northwest. Stress release from the foreshock prevents the mainshock from breaching the shallow portion of the orthogonal F2; instead a deep rupture pulse crosses the fault intersection, propagates again to the surface, and continues along F3 to its southeastern end. The mainshock reactivates slip on F2 near the intersection with F3 and dynamically triggers shallow slip at the southern end of F4.

2.3 Integrating an observationally constrained, complex fault damage zone

Fault zones are heterogeneous structures with variable degrees of rock damage (Peng et al., 2003; Cochran et al., 2009), and their properties can vary significantly along strike (Lewis & Ben-Zion, 2010; Materna & Bürgmann, 2016; Perrin et al., 2016). We complement the reference foreshock-mainshock dynamic rupture scenarios with an observation-

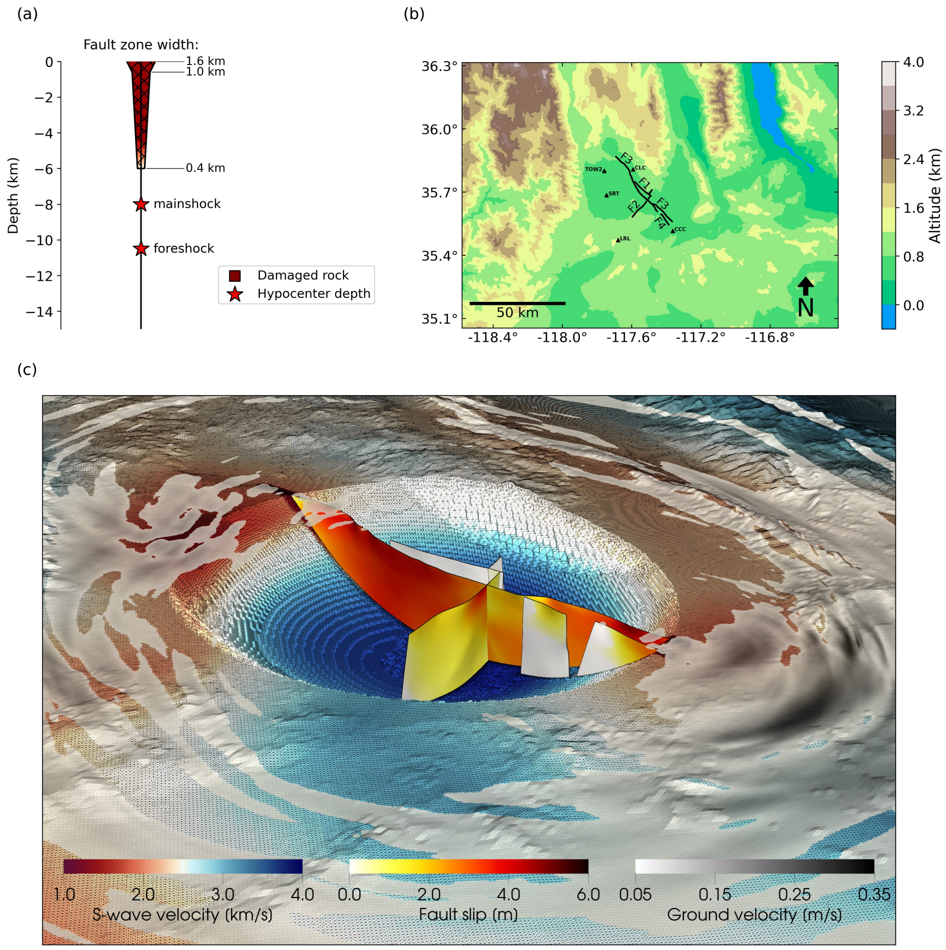

Figure 1. (a) Schematic of the flower-shaped fault damage zone geometry (Sec. 2.3) and hypocenter depths. (b) Map view showing model topography and fault traces, with F1, F2, F3, and F4 being the ruptured segments of the Ridgecrest fault system, following the reference foreshock-mainshock dynamic rupture models (Taufiqurrahman et al., 2023). Triangles indicate near-source station locations, for which synthetic and observed spectra are shown in Fig. S3 and S4. (c) Fault zone dynamic rupture model snapshot showing the combined fault slip (mainshock + foreshock) and absolute wave velocity 23 s after mainshock nucleation. The snapshot is cut out to illustrate the dynamic rupture models' complexities, including a quasi-orthogonal listric 3D fault system, high-resolution topography, 3D velocity structure merged with a shallow flower-shaped fault damage zone.

ally constrained fault damage zone representing an immature fault system with a rather low level of damage and localization (Ben-Zion & Sammis, 2003). To this end, we construct a shallow, flower-shaped fault damage zone geometry based on dense seismic observations, including four linear arrays crossing the surface ruptures, with 100 m sensor spacing (Qiu et al., 2021). Their derived fault zone structure includes a low-velocity zone with a width of 1–2 km, containing an intensely damaged core and a waveguide approximately 300 m wide, reaching depths of 3–5 km.

The modeled fault zone geometry follows the derived intensely damaged core of the low-velocity zone surrounding the Ridgecrest fault system. We approximate this complex structure with a flower-shaped geometry (Finzi et al., 2009; Pelties et al., 2015), neglecting along-strike variations (Huang, 2018). The fault-zone width is set to 1.6 km at the free surface, tapering to 1.0 km at 600 m depth, and further decreasing to 0.4 km at 6 km depth (Fig. 1a). Within this fault zone, we reduce P- and S-wave velocities from the 3D velocity model CVM-S4.26 (Lee et al., 2014) by 30%, with sharp lateral velocity contrasts at the fault zone edges. In the vertical direction, the velocity reduction occurs smoothly between depths of 4–6 km.

3 Results

We first compare the results of the FZ and reference models to investigate the impact of the fault zone on various ground motion parameters in Sec. 3.1. We aim to compare ground motion parameters of 3D dynamic rupture models that feature similar complexity as real earthquakes. Fig. S3 and S4 display synthetic and observed spectra of five near-source stations (Fig. 1b). The frequency content of the synthetic spectra compares well to the observations up to the model resolution of 2 Hz. After analyzing ground motion parameters, we examine the impact of the FZ structure on rupture dynamics in Sec. 3.2.

3.1 Fault zone impact on ground motions

Fig. 2 shows logarithmic ratios (e.g., Vach et al., 2021) of peak ground velocity (PGV) values generated by the FZ and reference models to analyze the spatial distribution of amplifications and deamplifications caused by the fault zone. Above rupturing faults, the FZ model generally generates higher PGVs (Ben-Zion et al., 2003; Catchings et al., 2020). The fault zone amplifies the PGVs more efficiently for the foreshock. In the near-field of the foreshock dynamic rupture scenario, the median PGV above the fault zone increases by 79%, from 0.47 m/s in the reference model to 0.84 m/s (Fig. 3a,b). The mainshock generates a median PGV of 1.19 m/s above the fault zone, representing a 19% increase compared to the median of 1.00 m/s of the reference model in the same area (Fig. 3c,d).

In the FZ model, we observe strong gradients in the fault-normal direction, where PGVs can change by a factor of 10 over a distance of 10 km. These results are consistent with recent work on an empirical ground motion model using aftershocks of the Ridgecrest earthquakes recorded by dense near-fault seismic arrays (Meng et al., 2024) and indicate propagation-site (rather than source) effects produced by the fault zone structure (Sec. 4).

Fig. S5 shows modeled PGVs on a regional scale and USGS intensity shakemaps (Wald et al., 2022) constructed from observations of the 2019 Ridgecrest sequence. Intensity-equivalent PGV values (Wald et al., 1999) are consistent with the results of the dynamic rupture simulations but feature less small-scale variability.

Details of rupture dynamics affect the trapping of waves in adjacent fault zones. During the foreshock, seismic waves are also amplified within the damage zones of the faults that will rupture only subsequently during the mainshock (F3 and F4), an effect that would have been missed when modeling rupture only on F1 and F2. This leads to a relative amplification of PGV by >2.2 at the southeastern end of the Ridgecrest fault system (Fig. 2a), more than 10 km away from the foreshock rupture (Marra et al., 2000; Rovelli et al., 2002). In contrast, during the mainshock, we do not observe an equivalent amplification (Fig. 2c). The mainshock tunnels the F2-F3 intersection (see 5–7 s in Movie S1 below the fault zone, preventing efficient trapping of waves within the damage zone of the orthogonal fault branch F2 (Taufiqurrahman et al., 2023).

Rupturing of adjacent fault zone regions that concentrate seismic energy shields neighboring regions from strong ground motions to some extent. For example, foreshock PGVs exhibit a relative reduction by >1.8 in the vicinity of strong amplification at the southeastern end of F3 (Fig. 2a).

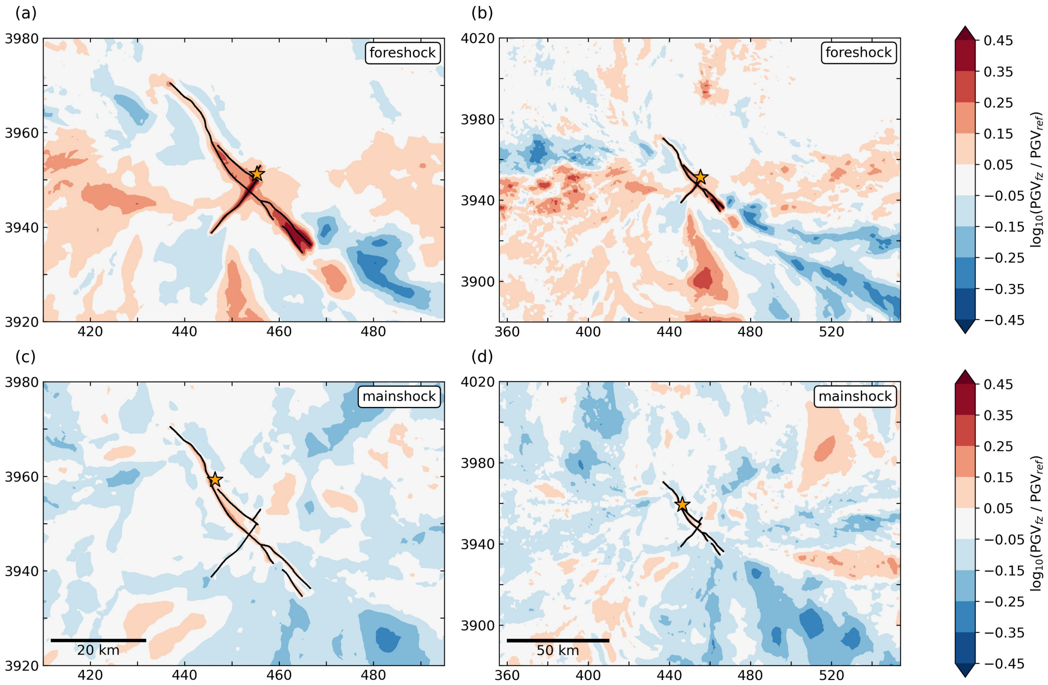

Figure 2. Logarithmic ratios of peak ground velocities $\log_{10}(\mathrm{PGV}_{fz}/\mathrm{PGV}_{ref})$ from two dynamic rupture models including a fault damage zone and the reference model. Logarithmic ratios indicate relative ground motion amplification and reduction, with values of ±0.05, ±0.25, and ±0.45 corresponding to factors of 1.12, 1.78, and 2.82, respectively. We use orientation-independent GMRotD50 PGV values (Boore et al., 2006). The coordinates are UTM 11S in km. (a) Near-fault distribution of the Searles Valley foreshock scenario. (b) Same as (a) but for a larger region. (c) Near-fault distribution of the Ridgecrest mainshock scenario. (d) Same as (c) but for a larger region.

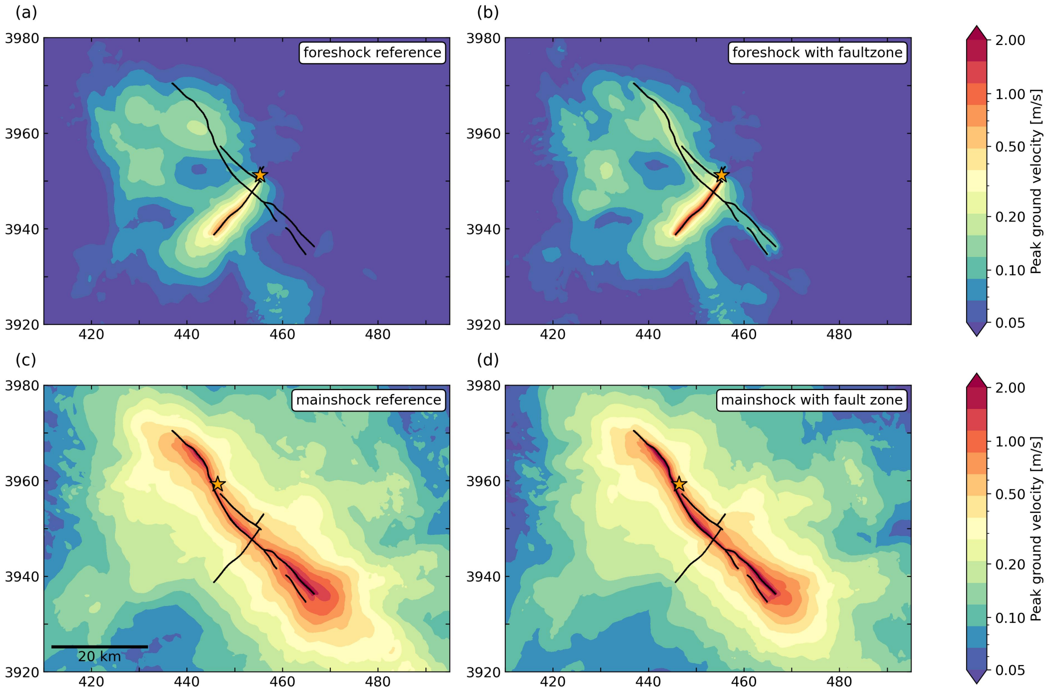

Figure 3. Near-fault PGV distributions of the (a) Searles Valley foreshock reference dynamic rupture model. (b) Searles Valley foreshock dynamic rupture model including a fault damage zone. (c) Ridgecrest mainshock reference dynamic rupture model. (d) Ridgecrest mainshock dynamic rupture model including a fault damage zone. We use orientation-independent GMRotD50 PGV values (Boore et al., 2006). The coordinates are UTM 11S in km.

The distortion of the near-source wavefield and altered rupture dynamics due to the fault zone (Sec. 3.2) considerably affect ground motions at distances beyond 100 km. Fig. 2b,d present logarithmic PGV ratios of the FZ relative to the reference model over distances up to 140 km. Amplification and deamplification patterns of both events are highly heterogeneous, with substantial variability over short distances. Yeh and Olsen (2023) found a similar regional-scale impact when simulating a kinematic source with and without surrounding fault zone structures.

We observe opposite fault zone effects on median PGVs during the foreshock and mainshock, highlighting event-specific and frequency dependence of fault zone effects that we detail when looking at peak spectral accelerations. Across the entire domain (Fig. 2b,d), the FZ model reduces the mainshock median PGV by 9.4% and increases the foreshock's median PGV by 2.2% compared to the reference model. The logarithmic PGV ratios have a standard deviation from zero of 0.090 for the mainshock and 0.105 for the foreshock, respectively, indicating a stronger FZ influence on foreshock ground motions also on a regional scale. Beyond the near-fault region, foreshock PGV ratios show pronounced amplification at angles of approximately $\pm 45°$ to the rupture forward direction, reflecting the mostly unilateral propagation along F2. A similar but weaker pattern is observed near both ends of F3 for the bilateral mainshock. These effects of the fault zone guided waves are distinct from the signatures of the radiation pattern of local impulsive vertical waves analyzed in (Schliwa & Gabriel, 2023).

The influence of the fault zone structure on ground motions is more pronounced at higher frequencies. Fig. 4 shows logarithmic ratios of the FZ and reference models' peak spectral accelerations (PSAs) at 3 s and 1 s (Boore et al., 2006). The different statistical spreads of the sets of logarithmic ratios quantify the relative fault zone impact on different frequency bands. For the foreshock, the logarithmic PSA ratio standard deviations from zero are 0.095 at 3 s and 0.173 at 1 s, with the latter corresponding to a relative PSA change by 1.49, representing de-/amplification by $\times 1.49$. The logarithmic PSA ratio standard deviations from zero for the mainshock are 0.119 at 3 s and 0.126 at 1 s, respectively. The values show that the relative impact on PSA_{1s} is higher for both events and particularly pronounced for the foreshock. While the large-scale amplification patterns of PSA ratios at 1 s and 3 s are largely consistent, they diverge in certain regions, such as south of the fault system at UTM x = 455 km for the mainshock. These

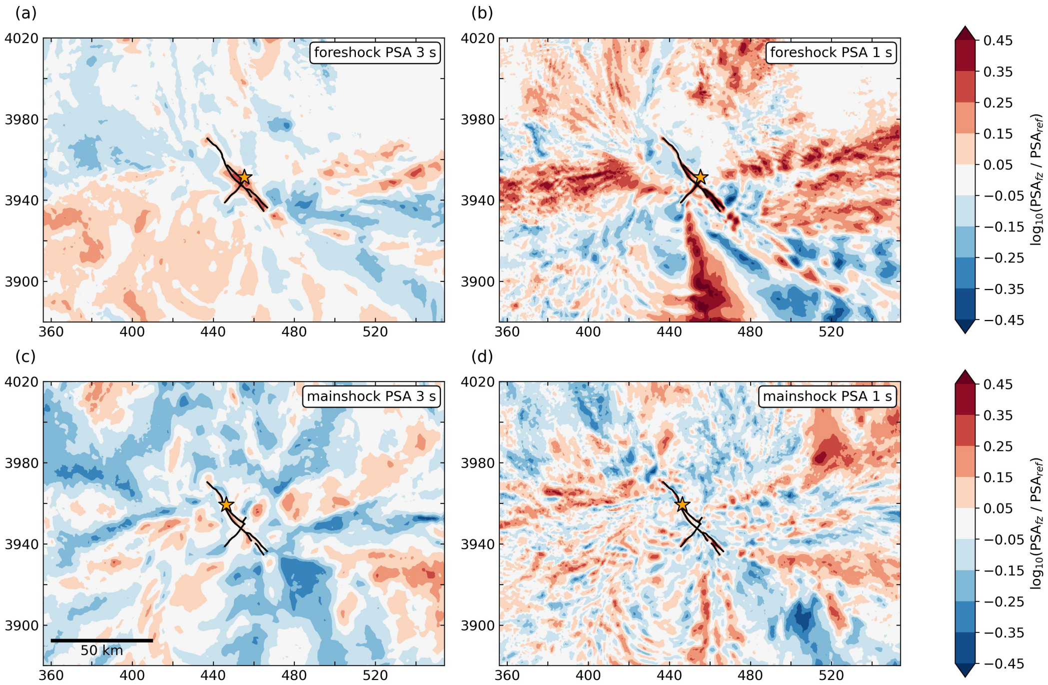

Figure 4. Logarithmic ratios of peak spectral accelerations (GMRotD50, Boore et al., 2006) comparing dynamic rupture models with a fault damage zone to the reference model. Logarithmic ratios indicate relative ground motion amplification and reduction, with values of ±0.05, ±0.25, and ±0.45 corresponding to factors of 1.12, 1.78, and 2.82, respectively. A high degree of saturation in diverging colorbar directions indicates a strong relative impact due to the fault zone. The coordinates are UTM 11S in km. (a) Period of 3 s, Searles Valley foreshock. (b) Period of 1 s, Searles Valley foreshock. (c) Period of 3 s, Ridgecrest mainshock. (d) Period of 1 s, Ridgecrest mainshock.

differences stem from the PSA_{1s} amplifications at angles of approximately ±45° from the southern end of F3 associated with the rupture directivity within the fault zone.

The frequency-dependency of the fault zone impact is related to the fault zone geometry and material properties. Fault zone trapped waves form due to constructive interference at the eigenfrequencies of the fault zone (Flores-Cuba et al., 2024; Ben-Zion, 1998); therefore, frequencies equal and higher than the fundamental eigenfrequency are affected the most. The fundamental eigenfrequency of a standing wave across the fault zone width w_{fz} with two fixed ends is $f_{fz} = v_s/(2w_{fz}) = 0.53\,\text{Hz}$, for $v_s = 1700\text{m/s}$ and $w_{fz} = 1600\text{m}$, corresponding to the average values at the free surface.

3.2 Fault zone impact on rupture dynamics

We compare the reference model of the 2019 Ridgecrest sequence (Taufiqurrahman et al., 2023) with the FZ model to investigate the fault zone's impact on rupture dynamics. Both dynamic rupture models share equivalent setups apart from the fault zone. Details of the reference model setup, a description of its rupture dynamics, and a visualization of the rupture evolution are provided in Sec. 2.1, 2.2, and Fig. S1, respectively. The analysis focuses on the mainshock, with foreshock results presented in the supplementary materials (Fig. S6–S8).

Fault zone waves and the reduction of the shear modulus within the fault zone considerably alter the final slip distribution of the mainshock model. Fig. 5 shows the potency and moment release rates of the reference and the FZ model, the accumulated fault slip in the FZ model, and the difference between the FZ and reference models' accumulated fault slip. In the FZ model, the accumulated slip is generally higher than in the reference model, which is reflected by an increase in the total potency. The assumed shear modulus reduction outweighs the slip increase and results in a lower seismic moment for both the mainshock and foreshock FZ model (Fig. S6). However, this is misleading in relation to the ground motion since the assumed rigidity at the source does not directly affect the radiated energy (Ben-Zion, 1989, 2001; Trugman & Ben-Zion, 2024), which is properly quantified by the potency. Slipping fault portions in the FZ mainshock model accumulate on average 2 m of slip, reaching maximum values of 5 m at the free surface near the southeastern end of F3. Within the fault zone near the hypocenter, slip increases by 0.3–0.4 m relative to the reference model.

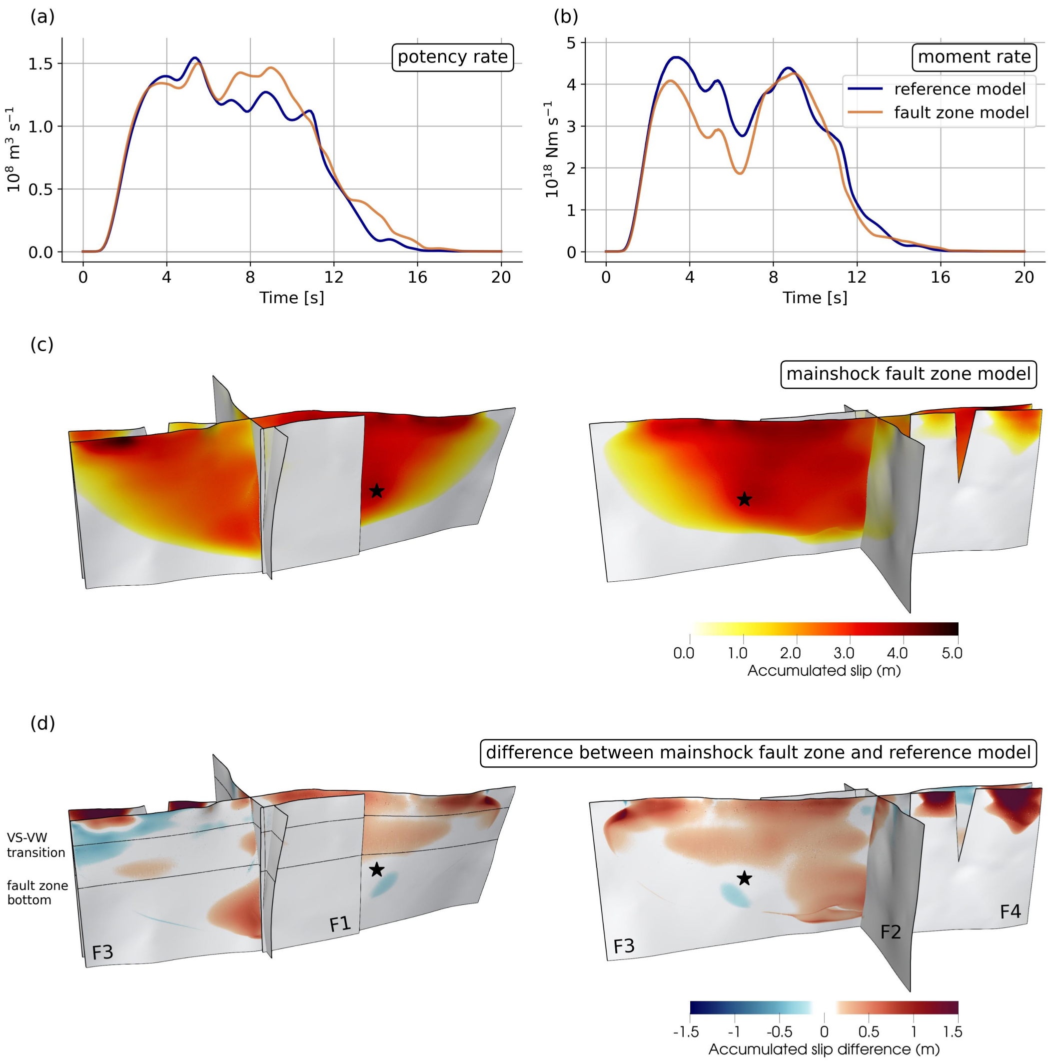

Figure 5. Comparison of rupture parameters in Ridgecrest mainshock models with and without the fault damage zone. (a) Potency release rate. (b) Moment release rate. (c) Accumulated slip distribution of the dynamic rupture model including the fault damage zone, showing two perspectives. (d) Difference in accumulated slip ($s_{fz} - s_{ref}$) of the dynamic rupture model, including the fault damage zone compared to the reference model. Contours indicate the velocity-strengthening to velocity-weakening transition (at a depth of 1.8 km), and the base of the fault zone (at 6 km depth).

The shallow fault zone structure amplifies surface-reflected rupture fronts, contributing to the accumulated slip increase. At the free surface, the FZ model's slip amplification grows with lateral distance from the hypocenter in both directions due to an amplified surface-reflected rupture front (e.g., Kaneko & Goto, 2022). Below the fault zone, slip differences between the FZ and the reference model are minimal, except near the F2-F3 intersection. In this region, the amplified surface-reflected rupture front originating from the hypocenter reaches the base of the seismogenic zone and even reinitiates rupture through the intersection with F2 for a second time (see 6–12 s in Movie S1).

On the southern segment of F3, the FZ model exhibits vertical and lateral oscillations of accumulated slip amplification and deamplification relative to the reference model (Fig. 5d). A superposition of fault zone waves generated at the southern F3 segment and those originating from the hypocentral region causes these complex oscillations. Rupture tunneling at the F2-F3 intersection and the associated delay lead to the rupture arriving at the southern F3 segment fault zone simultaneously with a pronounced fault zone wave packet emanating from the hypocentral region (30–36 s in Movie S2). The sign of the accumulated slip change depends on whether the dynamic stress perturbations due to fault zone waves favor slip when interacting with the rupture front. Reversed polarity slip reactivation (Glastonbury-Southern et al., 2022; P. M. Shearer et al., 2024) due to fault zone coda waves further contributes to the strong positive slip anomaly at the free surface of the southern F3 segment. We detail the slip reactivation and the time-dependent interactions between rupture and dynamic stress perturbations at the end of this section. Next to the southern segment of F3, fault zone waves dynamically trigger more shallow slip on F4 in the FZ model compared to the reference model.

Peak slip rates show a pronounced depth-dependent increase within the fault zone (Fig. 6 and S9). On average, peak slip rates within the fault zone are 70% higher than in the reference model, marking the most significant relative change induced by the fault zone. The largest changes occur in the velocity-weakening bottom half of the fault zone. We note that there the difference between the direct effect parameter and the state-evolution parameter $a - b$ is -0.004. The transition between seismogenic velocity-weakening and shallow velocity-strengthening frictional regimes falls between depths of 4 km and 1.8 km (Fig. S2), which aligns with a secondary shallow depth-dependent change in peak slip rate increase (Fig. 6a). Including the fault zone increases the spatial correlation of peak slip rates with accumulated slip, rise time, and rupture speed normalized by the rigid-

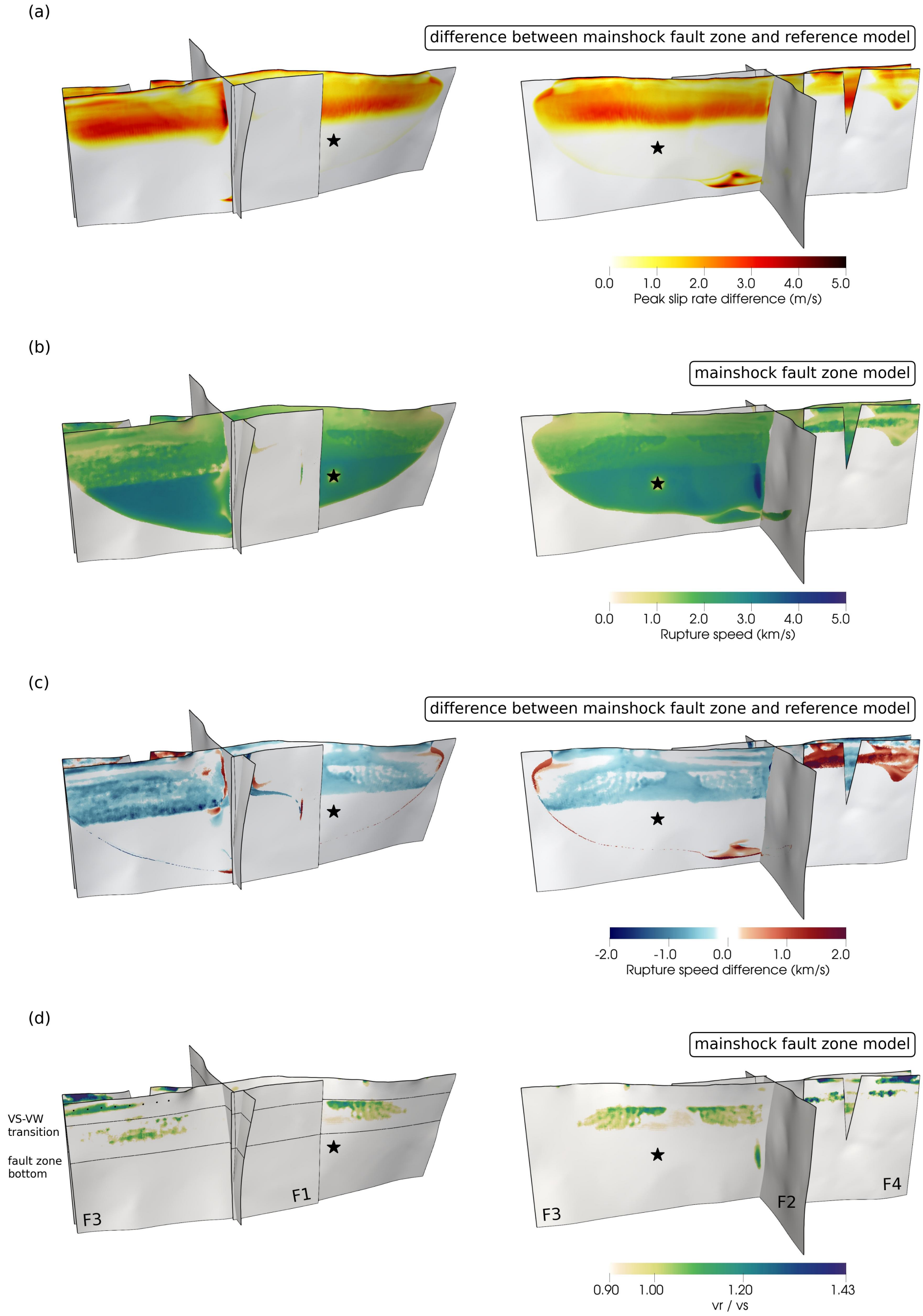

Figure 6. Comparison of Ridgecrest mainshock rupture dynamics in models with and without the fault damage zone, with each subplot showing two perspectives. (a) Difference in peak slip rate ($\max(\dot{s}_{fz}) - \max(\dot{s}_{ref})$). (b) Rupture speed distribution of the Ridgecrest mainshock FZ model. (c) Difference in rupture speed ($v_{r,fz} - v_{r,ref}$). (d) Ratio between rupture speed and local S-wave velocity ($v_{r,fz}/v_s$) of the Ridgecrest mainshock FZ model. The colorbar is saturated to highlight supershear rupture. Contours indicate the depth of the velocity-strengthening to velocity-weakening transition (1.8 km) and the bottom of the fault zone (6 km). Black dots in (d) show fault receiver locations analyzed in Fig. 7.

ity (Fig. S10). In particular, peak slip rate and rupture speed strongly correlate (> 0.8) for both foreshock and mainshock FZ models. This correlation appears to be dynamically enforced independently of the friction law (e.g., Schmedes et al., 2010; Schliwa et al., 2024).

Peak slip rates on the shallow southern segment of F3 show oscillations similar to the slip differences caused by fault zone trapped waves. However, unlike the slip differences, peak slip rates do not decrease compared to the reference model, and the oscillations do not align spatially with those of the accumulated slip differences. The spatial offsets arise from the accumulated slip being affected by slip reactivation due to fault zone coda waves (Fig. 7).

The fault damage zone facilitates supershear rupture, which is primarily confined to its bottom half. Within the fault zone, rupture speed decreases by an average of 17% compared to the reference model (Fig. 6c), which is less than the 30% reduction in seismic wave propagation velocities within the fault zone. These rupture speed changes have only a small effect on rupture duration (see Fig. 5a,b). Fig. 6d shows the ratio of rupture speed to local shear wave velocity, revealing localized, episodic supershear transitions at the bottom of the fault zone.

Episodic supershear rupture remains mostly confined to depths of 3-6 km, the velocity-weakening frictional regime within the fault zone (Cui & Zhu, 2022). However, a thin yet laterally stable supershear corridor exists at the southern end of F3, just below the free surface. This supershear rupture is induced within the velocity-strengthening regime due to a combination of rupture directivity, free surface reflections (Olsen et al., 1997; Kaneko & Lapusta, 2010; F. Hu et al., 2019), a superposition of fault zone waves generated in the adjacent fault zone and the hypocentral region (Huang et al., 2016), and wave focusing due to the slope change of the flower structure geometry (Fig. 1a Pelties et al., 2015).

Average rise times within the fault zone are reduced by 10% compared to the reference model when areas with long rise times due to surface reflections are excluded (see Fig. S11, which is less than observed for simpler dynamic rupture models incorporating a fault zone (Huang & Ampuero, 2011; Pelties et al., 2015).

Lateral oscillations of dynamic source parameters along the southern F3 segment are explained by the timing between the rupture front and dynamic stress perturbations due to fault zone waves. Fig. 7 shows normalized shear stress and slip rate evolution of eight fault receivers located along a constant-depth profile overlapping with the previously identified supershear corridor (Fig. 6d). Oscillations before and higher frequent shear stress modulations after the rupture onset represent dynamic perturbations due to fault zone waves. The first three fault receivers (a–c) have subshear rupture speeds, and a peak slip rate increases $\Delta\max(\dot{s}) <= 1$ m/s compared to the reference model. The subsequent receivers (d–g) exhibit supershear and larger increases in peak slip rate. For the fault receivers a–c, dynamic stress perturbations right before rupture onset are decreasing but do not turn negative, which indicates that the maximum unfavorable stress perturbations coincide with rupture onset. For the remaining receivers, the maximum unfavorable stress perturbations occur right before rupture onset, which then aligns with a favorable stress perturbation, facilitating supershear and large peak slip rate increases. We do not observe a daughter crack (Andrews, 1976; Burridge et al., 1979) during the supershear transition. Receivers e–g show notable reverse slip reactivations by fault zone coda waves, adding to the accumulated slip difference compared to the reference dynamic rupture model (Fig. 5d).

4 Discussion

The dynamic rupture models of the 2019 Ridgecrest sequence demonstrate that the shallow fault zone structure significantly impacts key aspects of the ruptures and ground motions up to regional distances. The effects are more substantial for high-frequency ground motions (> 0.5 Hz) and ground motions of the foreshock (Fig. 4). The corner frequencies of both events are lower than the fundamental eigenfrequency of the fault zone, but the foreshock of the Ridgecrest sequence has a higher corner frequency than the mainshock (Schliwa & Gabriel, 2023). Therefore, more of the foreshock's relative frequency content overlaps with the eigenfrequencies of the fault zone, which explains the stronger impact on the foreshock ground motions. This implies a magnitude dependence of the fault zone impact, which should reach its maximum when the events corner frequency exceeds the fundamental eigenfrequency of the fault zone. However, when the magnitude gets smaller it becomes less likely that the earthquake will rupture the Earth's surface (Bonilla, 1988; Wells & Coppersmith, 1994) and the shallow velocity-strengthening

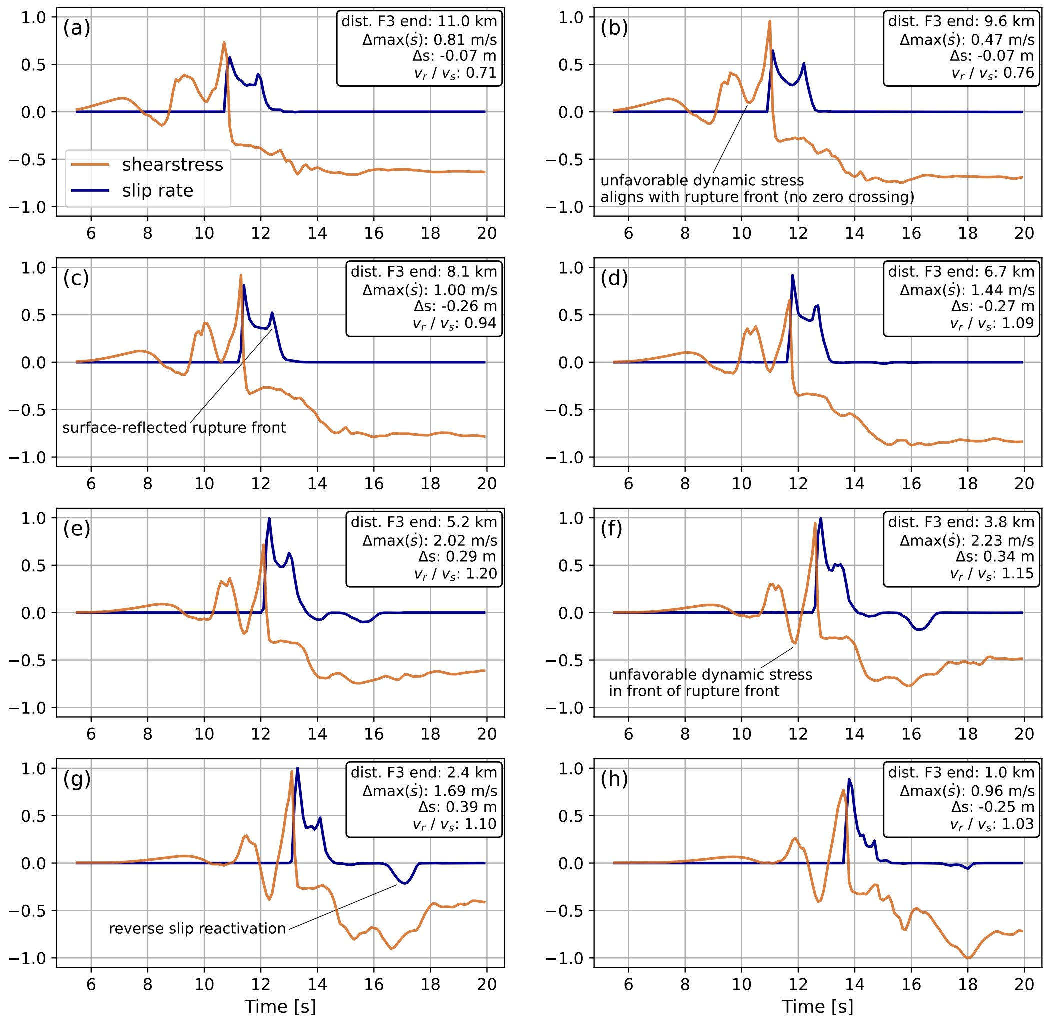

Figure 7. Normalized shear stress and slip rate evolution of the Ridgecrest mainshock model including the fault damage zone at eight fault receivers (a–h). The receivers are located along a constant depth profile (≈ 800 m) overlapping with the supershear corridor at the southern end of F3 (Fig. 6d). Insets show the distance to the southern end of F3, the difference in peak slip rate (Δmax($\dot{s}$)) and accumulated slip (Δs) compared to the reference mainshock model, and the ratio between rupture speed and local shear wave velocity (v_r/v_s), indicating supershear onset at the fault receiver associated with subplot (d).

and fault zone region. In addition, the higher frequencies generated by smaller events attenuate more along the same propagation distance.

Meng et al. (2024) analyze ground motion parameters of aftershocks of the Ridgecrest sequence with dense 1D arrays (Qiu et al., 2021) across the fault zone of the mainshock rupture. They observe ground motion parameter attenuation rates of aftershocks within the fault zone that are consistent with our simulated results for the FZ dynamic rupture models. The similar attenuation rates of ground motions from small and large events indicate that propagation rather than source effects dominate the fault zone's impact on the ground motions.

The shallow nature of fault damage zones may prevent extensive supershear rupture due to the overlap with the transition of the frictional regime. Observed coherent fault zone waveguides, capable of generating fault zone trapped waves, typically extend to depths of only 3–5 km (e.g., Ben-Zion et al., 2003; Lewis et al., 2005; Lewis & Ben-Zion, 2010; Qiu et al., 2021). Evidence for shallow velocity-strengthening portions (Kaneko et al., 2008) of strike-slip fault systems include the lack of shallow seismicity (e.g., P. Shearer et al., 2005; Peng & Zhao, 2009), the coseismic shallow slip deficit (e.g., Fialko et al., 2005), and shallow afterslip following large earthquakes (e.g., Hsu et al., 2006; Barbot et al., 2012). Laboratory experiments and in-situ observations associate this shallow velocity-strengthening zone with unconsolidated sediments and fault gouge (e.g., C. J. Marone et al., 1991; Chester et al., 1993; Beeler et al., 1996; C. Marone, 1998; Lockner et al., 2011). The dynamic rupture models indicate that such a shallow transition to velocity-strengthening friction inhibits sustained supershear rupture within the fault zone. This suggests that fault zone-induced supershear transitions may be less common than predicted by numerical studies assuming constant friction parameters (Huang et al., 2014, 2016). Nonetheless, the FZ model produces supershear rupture speeds in a thin corridor close to the free surface at the southeastern end of the mainshock rupture, even within the velocity-strengthening regime (Fig. 7). Loading and unloading waves reflected from 3D material heterogeneities can further complicate supershear transitions, even when the heterogeneities occur at some distance from the fault surface (Ma & Elbanna, 2015).

Dynamic stress perturbations due to fault zone waves can be crucial for dynamically activating secondary faults. We find (Fig. 5d) that fault zone waves dynamically trigger substantial rupture along F4 while assuming identical frictional conditions for F3 and F4. The additional triggered slip aligns with Ridgecrest mainshock observations that indicate that F4 experienced anelastic damage, surface rupture, and localized aftershock activity (Ross et al., 2019; Milliner & Donnellan, 2020).

We assume a coherent pre-existing fault damage zone, which might be exaggerated compared to natural conditions. However, low-velocity zones around faults generated by previous ruptures remain for a long time (e.g., Rovelli et al., 2002), suggesting that fault damage zones likely existed around the main ruptures prior to the Ridgecrest sequence. The limited data near the rupture zones, where the fault zone effects are most pronounced, prevents us from performing a detailed comparison of simulation results to observations and highlights the need for additional near-fault sensors (e.g., Ben-Zion, 2019). The small-scale variability introduced by the fault zone structure further highlights the need for dense recordings to quantify the source and near-source effects.

5 Conclusions

We analyze the effects of a shallow flower-shaped fault zone in linked dynamic rupture models of the 2019 Ridgecrest sequence on the generated ground motions and rupture dynamics. The combination of the fault zone's near-source wavefield distortion and rupture dynamic changes considerably affects ground motions locally and beyond distances of 100 km. The impact on ground motions is frequency- and magnitude-dependent, which is related to the difference between an event's corner frequency and eigenfrequencies of the fault zone structure. The shallow fault zone geometry and the shallow transition to velocity-strengthening friction confine fault zone-induced supershear rupture to localized areas in the FZ dynamic rupture model. While v_s within the fault zone is reduced by 30%, the rupture speed is reduced on average by 17%, reflecting the local increase of v_r/v_s. Peak slip rates within the fault zone exhibit the most extreme relative change, with an average increase of 70% compared to the reference model. The shallow fault zone amplifies surface-reflected rupture fronts, enabling a secondary surface-reflected rupture front of the Ridgecrest mainshock FZ model to re-rupture the base of the seismogenic zone. The reduced rigidity leads to lower seismic moments for both the FZ foreshock and mainshock models, despite an increase in seismic potency, which is more fundamentally related to seismic radiation. These results highlight the importance of near-source velocity structure for local and regional-scale ground motion modeling and physics-based seismic hazard assessments.

Open Research Section

The open-source dynamic rupture software SeisSol is available at `https://seissol.org/`. The setup to run the reference Ridgecrest model is available at Zenodo (Taufiqurrahman, Gabriel, Li, et al., 2022a), as well as the associated SeisSol version (Taufiqurrahman, Gabriel, Li, et al., 2022b), and the material files to incorporate the low-velocity fault zone (Schliwa, 2024). We compute ground motion parameters with the following script: `https://github.com/SeisSol/SeisSol/tree/master/postprocessing/science/GroundMotionParametersMaps`. All seismic data were accessed through the IRIS Wilber 3 system (`https://ds.iris.edu/wilber3/`) from the Southern California Seismic Network (CI, California Institute of Technology and United States Geological Survey Pasadena, 1926). The Python package ObsPy was used to remove the instrument response (Krischer et al., 2015).

Acknowledgments

The authors declare no conflict of interest. We thank Taufiqurrahman for providing and discussing his dynamic rupture models. This study was supported by Horizon Europe (ChEESE-2P, grant number 101093038, DT-GEO, grant number 101058129, and Geo-INQUIRE, grant number 101058518), the Deutsche Forschungsgemeinschaft (DFG, German Research Foundation, grant numbers 495931446, 518204048), the National Aeronautics and Space Administration (80NSSC20K0495), the National Science Foundation (grant numbers EAR-2225286, EAR-2121568, OAC-2139536, OAC-2311208, OAC-2311206) and the Southern California Earthquake Center (SCEC awards 22135, 23121). We thank the Gauss Centre for Supercomputing e.V. (`www.gauss-centre.eu`) for providing us with computing time on the supercomputer SuperMUC-NG at the Leibniz Supercomputing Centre (`www.lrz.de`) in projects pr63qo, pn49ha. Additional computing resources were provided by the Institute of Geophysics of LMU Munich (Oeser et al., 2006).

References

Abdelmeguid, M., & Elbanna, A. (2022). Modeling Sequences of Earthquakes and Aseismic Slip (SEAS) in Elasto-Plastic Fault Zones With a Hybrid Finite Element Spectral Boundary Integral Scheme. *Journal of Geophysical Research: Solid Earth*, *127*(12).

Allam, A., Ben-Zion, Y., & Peng, Z. (2014). Seismic Imaging of a Bimaterial Interface Along the Hayward Fault, CA, with Fault Zone Head Waves and Direct P

Arrivals. *Pure and Applied Geophysics*, *171*.

Andrews, D. J. (1976). Rupture velocity of plane strain shear cracks. *Journal of Geophysical Research (1896-1977)*, *81*(32), 5679-5687. doi: 10.1029/JB081i032p05679

Andrews, D. J., & Ben-Zion, Y. (1997). Wrinkle-like slip pulse on a fault between different materials. *Journal of Geophysical Research: Solid Earth*, *102*(B1).

Barbot, S., Lapusta, N., & Avouac, J.-P. (2012). Under the Hood of the Earthquake Machine: Toward Predictive Modeling of the Seismic Cycle. *Science*, *336*.

Beeler, N. M., Tullis, T. E., Blanpied, M. L., & Weeks, J. D. (1996). Frictional behavior of large displacement experimental faults. *Journal of Geophysical Research: Solid Earth*, *101*.

Ben-Zion, Y. (1989). The response of two joined quarter spaces to SH line sources located at the material discontinuity interface. *Geophysical Journal International*, *98*(2), 213-222. doi: 10.1111/j.1365-246X.1989.tb03346.x

Ben-Zion, Y. (1990). The response of two half spaces to point dislocations at the material interface. *Geophysical Journal International*, *101*(3).

Ben-Zion, Y. (1998). Properties of seismic fault zone waves and their utility for imaging low-velocity structures. *Journal of Geophysical Research: Solid Earth*, *103*(B6). doi: https://doi.org/10.1029/98JB00768

Ben-Zion, Y. (2001). On Quantification of the Earthquake Source. *Seismological Research Letters*, *72*(2), 151-152. doi: 10.1785/gssrl.72.2.151

Ben-Zion, Y., & Huang, Y. (2002). Dynamic rupture on an interface between a compliant fault zone layer and a stiffer surrounding solid. *Journal of Geophysical Research: Solid Earth*, *107*(B2).

Ben-Zion, Y., Peng, Z., Okaya, D., Seeber, L., Armbruster, J. G., Ozer, N., … Aktar, M. (2003). A shallow fault-zone structure illuminated by trapped waves in the Karadere–Duzce branch of the North Anatolian Fault, western Turkey. *Geophysical Journal International*, *152*.

Ben-Zion, Y., & Sammis, C. (2003). Characterization of Fault Zones. *Pure and Applied Geophysics*, *160*.

Ben-Zion, Y. (2019). A Critical Data Gap in Earthquake Physics. *Seismological Research Letters*, *90*(5), 1721-1722. doi: 10.1785/0220190167

Bonilla, M. G. (1988). Minimum Earthquake Magnitude Associated with Coseismic

Surface Faulting. *Environmental & Engineering Geoscience*, *xxv*(1), 17-29. doi: 10.2113/gseegeosci.xxv.1.17

Boore, D. M., Watson-Lamprey, J., & Abrahamson, N. A. (2006). Orientation-Independent Measures of Ground Motion. *Bulletin of the Seismological Society of America*, *96*.

Burridge, R., Conn, G., & Freund, L. B. (1979). The stability of a rapid mode II shear crack with finite cohesive traction. *Journal of Geophysical Research: Solid Earth*, *84*(B5), 2210-2222. doi: 10.1029/JB084iB05p02210

California Institute of Technology and United States Geological Survey Pasadena. (1926). Southern California Seismic Network. *International Federation of Digital Seismograph Networks*. doi: 10.7914/SN/CI

Carena, S., & Suppe, J. (2002). Three-dimensional imaging of active structures using earthquake aftershocks: The Northridge thrust, California. *Journal of Structural Geology*, *24*.

Catchings, R. D., Rymer, M. J., & Goldman, M. R. (2020). San Andreas Fault Exploration Using Refraction Tomography and S-Wave-Type and F_Φ-Mode Guided Waves. *Bulletin of the Seismological Society of America*, *110*(6).

Chen, K., Avouac, J.-P., Aati, S., Milliner, C., Zheng, F., & Shi, C. (2020). Cascading and pulse-like ruptures during the 2019 Ridgecrest earthquakes in the Eastern California Shear Zone. *Nature Communications*, *11*. doi: 10.1038/s41467-019-13750-w

Chester, F. M., Evans, J. P., & Biegel, R. L. (1993). Internal structure and weakening mechanisms of the San Andreas Fault. *Journal of Geophysical Research: Solid Earth*, *98*.

Cochran, E. S., Li, Y.-G., Shearer, P. M., Barbot, S., Fialko, Y., & Vidale, J. E. (2009). Seismic and geodetic evidence for extensive, long-lived fault damage zones. *Geology*, *37*.

Cormier, V. F., & Spudich, P. (1984). Amplification of ground motion and waveform complexity in fault zones: examples from the San Andreas and Calaveras Faults. *Geophysical Journal International*, *79*(1).

Cui, Z., & Zhu, S. (2022). Effect of real-world frictional strengthening layer near the Earth's free surface on rupture characteristics with different friction laws: Implication for scarcity of supershear earthquakes. *Tectonophysics*, *837*. doi:

10.1016/j.tecto.2022.229447

Dunham, E., Belanger, D., Cong, L., & Kozdon, J. (2011). Earthquake Ruptures with Strongly Rate-Weakening Friction and Off-Fault Plasticity, Part 1: Planar Faults. *Bulletin of The Seismological Society of America*, *101*.

Farr, T. G., Rosen, P. A., Caro, E., Crippen, R., Duren, R., Hensley, S., … Alsdorf, D. (2007). The Shuttle Radar Topography Mission. *Reviews of Geophysics*, *45*(2).

Fialko, Y., Sandwell, D., Simons, M., & Rosen, P. (2005). Three-dimensional deformation caused by the Bam, Iran, earthquake and the origin of shallow slip deficit. *Nature*, *435*.

Finzi, Y., Hearn, E., Ben-Zion, Y., & Lyakhovsky, V. (2009). Structural Properties and Deformation Patterns of Evolving Strike-slip Faults: Numerical Simulations Incorporating Damage Rheology. *Pure and Applied Geophysics*, *166*. doi: 10.1007/978-3-0346-0138-2_2

Flores-Cuba, J., Oral, E., Idini, B., Liang, C., & Ampuero, J. P. (2024). Mechanisms and Seismological Signatures of Rupture Complexity Induced by Fault Damage Zones in Fully-Dynamic Earthquake Cycle Models. *Geophysical Research Letters*, *51*.

Folch, A., Abril, C., Afanasiev, M., Amati, G., Bader, M., Badia, R. M., … Wössner, U. (2023). The EU Center of Excellence for Exascale in Solid Earth (ChEESE): Implementation, results, and roadmap for the second phase. *Future Generation Computer Systems*, *146*.

Glastonbury-Southern, E., Winder, T., White, R. S., & Brandsdóttir, B. (2022). Ring Fault Slip Reversal at Bárðarbunga Volcano, Iceland: Seismicity During Caldera Collapse and Re-Inflation 2014–2018. *Geophysical Research Letters*, *49*(21), e2021GL097613. doi: 10.1029/2021GL097613

Goldberg, D., Melgar, D., Sahakian, V., Thomas, A., Xu, X., Crowell, B., & Geng, J. (2020). Complex Rupture of an Immature Fault Zone: A Simultaneous Kinematic Model of the 2019 Ridgecrest, CA Earthquakes. *Geophysical Research Letters*, *47*. doi: 10.1029/2019GL086382

Hillers, G., Campillo, M., Ben-Zion, Y., & Roux, P. (2014). Seismic fault zone trapped noise. *Journal of Geophysical Research: Solid Earth*, *119*(7).

Hsu, Y.-J., Simons, M., Avouac, J.-P., Galetzka, J., Sieh, K., Chlieh, M., … Bock,

Y. (2006). Frictional Afterslip Following the 2005 Nias-Simeulue Earthquake, Sumatra. *Science*, *312*.

Hu, F., Oglesby, D. D., & Chen, X. (2019). The Sustainability of Free-Surface-Induced Supershear Rupture on Strike-Slip Faults. *Geophysical Research Letters*, *46*(16), 9537-9543. doi: 10.1029/2019GL084318

Hu, Z., Olsen, K. B., & Day, S. M. (2022). 0–5 Hz deterministic 3-D ground motion simulations for the 2014 La Habra, California, Earthquake. *Geophysical Journal International*, *230*(3).

Huang, Y. (2018). Earthquake Rupture in Fault Zones With Along-Strike Material Heterogeneity. *Journal of Geophysical Research: Solid Earth*, *123*(11), 9884-9898. doi: 10.1029/2018JB016354

Huang, Y., & Ampuero, J.-P. (2011). Pulse-like ruptures induced by low-velocity fault zones. *Journal of Geophysical Research: Solid Earth*, *116*(B12). doi: https://doi.org/10.1029/2011JB008684

Huang, Y., Ampuero, J.-P., & Helmberger, D. V. (2014). Earthquake ruptures modulated by waves in damaged fault zones. *Journal of Geophysical Research: Solid Earth*, *119*(4). doi: https://doi.org/10.1002/2013JB010724

Huang, Y., Ampuero, J.-P., & Helmberger, D. V. (2016). The potential for supershear earthquakes in damaged fault zones – theory and observations. *Earth and Planetary Science Letters*, *433*.

Igel, H., Jahnke, G., & Ben-Zion, Y. (2002). Numerical Simulation of Fault Zone Guided Waves: Accuracy and 3-D Effects. *Pure and Applied Geophysics*, *159*, 2067-2083.

Kaneko, Y., & Goto, H. (2022). The Origin of Large, Long-Period Near-Fault Ground Velocities During Surface-Breaking Strike-Slip Earthquakes. *Geophysical Research Letters*, *49*.

Kaneko, Y., & Lapusta, N. (2010). Supershear transition due to a free surface in 3-D simulations of spontaneous dynamic rupture on vertical strike-slip faults. *Tectonophysics*, *493*(3), 272-284. doi: https://doi.org/10.1016/j.tecto.2010.06.015

Kaneko, Y., Lapusta, N., & Ampuero, J.-P. (2008). Spectral element modeling of spontaneous earthquake rupture on rate and state faults: Effect of velocity-strengthening friction at shallow depths. *Journal of Geophysical Research:*

Solid Earth, *113*.

Krischer, L., Megies, T., Barsch, R., Beyreuther, M., Lecocq, T., Caudron, C., & Wassermann, J. (2015). ObsPy: A bridge for seismology into the scientific Python ecosystem. *Computational Science & Discovery*, *8*. doi: 10.1088/1749-4699/8/1/014003

Kurzon, I., Vernon, F., BenZion, Y., & Atkinson, G. (2014). Ground Motion Prediction Equations in the San Jacinto Fault Zone – Significant Effects of Rupture Directivity and Fault Zone Amplification. *Pure and Applied Geophysics*, *171*.

Lee, E.-J., Chen, P., Jordan, T. H., Maechling, P. B., Denolle, M. A. M., & Beroza, G. C. (2014). Full-3-D tomography for crustal structure in Southern California based on the scattering-integral and the adjoint-wavefield methods. *Journal of Geophysical Research: Solid Earth*, *119*.

Lewis, M. A., & Ben-Zion, Y. (2010). Diversity of fault zone damage and trapping structures in the Parkfield section of the San Andreas Fault from comprehensive analysis of near fault seismograms. *Geophysical Journal International*, *183*.

Lewis, M. A., Peng, Z., Ben-Zion, Y., & Vernon, F. L. (2005). Shallow seismic trapping structure in the San Jacinto fault zone near Anza, California. *Geophysical Journal International*, *162*.

Li, Y.-G., & Leary, P. C. (1990). Fault zone trapped seismic waves. *Bulletin of the Seismological Society of America*, *80*(5).

Liu, C., Lay, T., Brodsky, E. E., Dascher-Cousineau, K., & Xiong, X. (2019). Coseismic Rupture Process of the Large 2019 Ridgecrest Earthquakes From Joint Inversion of Geodetic and Seismological Observations. *Geophysical Research Letters*, *46*.

Lockner, D. A., Morrow, C., Moore, D., & Hickman, S. (2011). Low strength of deep San Andreas fault gouge from SAFOD core. *Nature*, *472*.

Ma, X., & Elbanna, A. (2015). Effect of off-fault low-velocity elastic inclusions on supershear rupture dynamics. *Geophysical Journal International*, *203*(1), 664-677. doi: 10.1093/gji/ggv302

Marone, C. (1998). Laboratory-derived friction laws and their application to seismic faulting. *Annual Review of Earth and Planetary Sciences*, *26*.

Marone, C. J., Scholtz, C. H., & Bilham, R. (1991). On the mechanics of earthquake afterslip. *Journal of Geophysical Research: Solid Earth*, *96*.

Marra, F., Azzara, R., Bellucci, F., Caserta, A., Cultrera, G., Mele, G., ... Boschi, E. (2000). Large amplification of ground motion at rock sites within a fault zone in Nocera Umbra (Central Italy). *Journal of Seismology*, *4*, 543-554. doi: 10.1023/A:1026559901378

Materna, K., & Bürgmann, R. (2016). Contrasts in compliant fault zone properties inferred from geodetic measurements in the San Francisco Bay area. *Journal of Geophysical Research: Solid Earth*, *121*(9), 6916-6931. doi: 10.1002/2016JB013243

Meng, X., Pinilla Ramos, C., Kottke, A. R., & Ben-Zion, Y. (2024). Developing a Near-fault Non-ergodic Ground Motion Model for the Ridgecrest, CA, Area. *Poster Presentation at 2024 SCEC Annual Meeting*.

Milliner, C., & Donnellan, A. (2020). Using Planet Labs Satellite Imagery to Separate the Surface Deformation Between the July 4th Mw 6.4 Foreshock and July 5th Mw 7.1 Mainshock During the 2019 Ridgecrest Earthquake Sequence. *Seismological Research Letters*, *91*. doi: 10.1785/0220190271

Oeser, J., Bunge, H.-P., & Mohr, M. (2006). Cluster design in the earth sciences tethys. In M. Gerndt & D. Kranzlmüller (Eds.), *High performance computing and communications.* Springer Berlin Heidelberg.

Olsen, K. B., Day, S. M., & Bradley, C. R. (2003). Estimation of Q for Long-Period ($>$ 2 sec) Waves in the Los Angeles Basin. *Bulletin of the Seismological Society of America*, *93*.

Olsen, K. B., Madariaga, R., & Archuleta, R. J. (1997). Three-Dimensional Dynamic Simulation of the 1992 Landers Earthquake. *Science*, *278*(5339), 834-838. doi: 10.1126/science.278.5339.834

Pelties, C., Huang, Y., & Ampuero, J.-P. (2015). Pulse-Like Rupture Induced by Three-Dimensional Fault Zone Flower Structures. *Pure Applied Geophysics*, *172*. doi: https://doi.org/10.1007/s00024-014-0881-0

Peng, Z., Ben-Zion, Y., Michael, A. J., & Zhu, L. (2003). Quantitative analysis of seismic fault zone waves in the rupture zone of the 1992 Landers, California, earthquake: evidence for a shallow trapping structure. *Geophysical Journal International*, *155*(3), 1021-1041. doi: 10.1111/j.1365-246X.2003.02109.x

Peng, Z., & Zhao, P. (2009). Migration of early aftershocks following the 2004 Parkfield earthquake. *Nature Geoscience*, *2*.

Perrin, C., Manighetti, I., Ampuero, J.-P., Cappa, F., & Gaudemer, Y. (2016). Location of largest earthquake slip and fast rupture controlled by along-strike change in fault structural maturity due to fault growth. *Journal of Geophysical Research: Solid Earth*, *121*(5), 3666-3685. doi: 10.1002/2015JB012671

Qiu, H., Allam, A. A., Lin, F.-C., & Ben-Zion, Y. (2020). Analysis of Fault Zone Resonance Modes Recorded by a Dense Seismic Array Across the San Jacinto Fault Zone at Blackburn Saddle. *Journal of Geophysical Research: Solid Earth*, *125*(10).

Qiu, H., Ben-Zion, Y., Catchings, R., Goldman, M. R., Allam, A. A., & Steidl, J. (2021). Seismic Imaging of the Mw 7.1 Ridgecrest Earthquake Rupture Zone From Data Recorded by Dense Linear Arrays. *Journal of Geophysical Research: Solid Earth*, *126*(7). doi: 10.1029/2021JB022043

Rodgers, A. J., Pitarka, A., Pankajakshan, R., Sjögreen, B., & Petersson, N. A. (2020). Regional-Scale 3D Ground-Motion Simulations of Mw 7 Earthquakes on the Hayward Fault, Northern California Resolving Frequencies 0–10 Hz and Including Site-Response Corrections. *Bulletin of the Seismological Society of America*, *110*(6).

Ross, Z. E., Idini, B., Jia, Z., Stephenson, O. L., Zhong, M., Wang, X., … Jung, J. (2019). Hierarchical interlocked orthogonal faulting in the 2019 Ridgecrest earthquake sequence. *Science*, *366*(6463). doi: 10.1126/science.aaz0109

Rovelli, A., Caserta, A., Marra, F., & Ruggiero, V. (2002). Can Seismic Waves Be Trapped inside an Inactive Fault Zone? The Case Study of Nocera Umbra, Central Italy. *Bulletin of the Seismological Society of America*, *92*(6), 2217-2232. doi: 10.1785/0120010288

Sammis, C., Rosakis, A., & Bhat, H. (2009). Effects of Off-fault Damage on Earthquake Rupture Propagation: Experimental Studies. *Pure and Applied Geophysics*, *166*.

Schliwa, N. (2024). *Fault zone material files for dynamic rupture modeling of the 2019 Ridgecrest earthquakes* [Dataset]. Zenodo. doi: 10.5281/zenodo.7352554

Schliwa, N., & Gabriel, A. (2023). Equivalent Near-Field Corner Frequency Analysis of 3D Dynamic Rupture Simulations Reveals Dynamic Source Effects. *Seismological Research Letters*, *95*.

Schliwa, N., Gabriel, A.-A., Premus, J., & Gallovič, F. (2024). The Linked Complexity of Coseismic and Postseismic Faulting Revealed by Seismo-Geodetic Dynamic Inversion of the 2004 Parkfield Earthquake. *Journal of Geophysical Research: Solid Earth*, *129*(12), e2024JB029410. doi: 10.1029/2024JB029410

Schmedes, J., Archuleta, R. J., & Lavallée, D. (2010). Correlation of earthquake source parameters inferred from dynamic rupture simulations. *Journal of Geophysical Research: Solid Earth*, *115*(B3). doi: 10.1029/2009JB006689

Shearer, P., Hauksson, E., & Lin, G. (2005). Southern California Hypocenter Relocation with Waveform Cross-Correlation, Part 2: Results Using Source-Specific Station Terms and Cluster Analysis. *Bulletin of the Seismological Society of America*, *95*.

Shearer, P. M., Shabikay Senobari, N., & Fialko, Y. (2024). Implications of a Reverse Polarity Earthquake Pair on Fault Friction and Stress Heterogeneity Near Ridgecrest, California. *Journal of Geophysical Research: Solid Earth*, *129*(11), e2024JB029562. doi: 10.1029/2024JB029562

Small, P., Gill, D., Maechling, P., Taborda, R., Callaghan, S., Jordan, T., … Goulet, C. (2017). The SCEC Unified Community Velocity Model Software Framework. *Seismological Research Letters*, *88*. doi: 10.1785/0220170082

Taufiqurrahman, T., Gabriel, A.-A., Li, D., Ulrich, T., Li, B., Carena, S., … Gallovič, F. (2022a). *Dynamic Rupture Modeling of the 2019 Ridgecrest Earthquakes* [Dataset]. Zenodo. doi: 10.5281/zenodo.7352554

Taufiqurrahman, T., Gabriel, A.-A., Li, D., Ulrich, T., Li, B., Carena, S., … Gallovič, F. (2022b). *Ridgecrest setup SeisSol source code* [Software]. Zenodo. doi: 10.5281/zenodo.7642533

Taufiqurrahman, T., Gabriel, A.-A., Li, D., Ulrich, T., Li, B., Carena, S., … Gallovič, F. (2023). Dynamics, interactions and delays of the 2019 Ridgecrest rupture sequence. *Nature*. doi: 10.1038/s41586-023-05985-x

Taufiqurrahman, T., Gabriel, A.-A., Ulrich, T., Valentová, L., & Gallovič, F. (2022). Broadband Dynamic Rupture Modeling With Fractal Fault Roughness, Frictional Heterogeneity, Viscoelasticity and Topography: The 2016 Mw 6.2 Amatrice, Italy Earthquake. *Geophysical Research Letters*, *49*(22).

Thakur, P., Huang, Y., & Kaneko, Y. (2020). Effects of Low-Velocity Fault Damage Zones on Long-Term Earthquake Behaviors on Mature Strike-

Slip Faults. *Journal of Geophysical Research: Solid Earth*, *125*(8). doi: https://doi.org/10.1029/2020JB019587

Trugman, D. T., & Ben-Zion, Y. (2024). Potency–Magnitude Scaling Relations and a Unified Earthquake Catalog for the Western United States. *The Seismic Record*, *4*(3), 223-230. doi: 10.1785/0320240022

Ulrich, T., Gabriel, A., Ampuero, J. P., & Xu, W. (2019). Dynamic viability of the 2016 Mw 7.8 Kaikōura earthquake cascade on weak crustal faults. *Nature Communications*, *10*.

Uphoff, C., Rettenberger, S., Bader, M., Madden, E. H., Ulrich, T., Wollherr, S., & Gabriel, A.-A. (2017). Extreme scale multi-physics simulations of the tsunamigenic 2004 sumatra megathrust earthquake. In *Proceedings of the international conference for high performance computing, networking, storage and analysis* (p. 21).

Vach, K., Al-Ahmad, A., Anderson, A., Woelber, J. P., Karygianni, L., Wittmer, A., & Hellwig, E. (2021). A Log Ratio-Based Analysis of Individual Changes in the Composition of the Oral Microbiota in Different Dietary Phases. *Nutrients*, *13*(3), 793. doi: 10.3390/nu13030793

Verdecchia, A., & Carena, S. (2016). Coulomb stress evolution in a diffuse plate boundary: 1400 years of earthquakes in eastern California and western Nevada, USA. *Tectonics*, *35*.

Wald, D. J., Quitoriano, V., Heaton, T. H., & Kanamori, H. (1999). Relationships between Peak Ground Acceleration, Peak Ground Velocity, and Modified Mercalli Intensity in California. *Earthquake Spectra*, *15*(3), 557-564. doi: 10.1193/1.1586058

Wald, D. J., Worden, C. B., Thompson, E. M., & Hearne, M. (2022). ShakeMap operations, policies, and procedures. *Earthquake Spectra*, *38*(1), 756-777. doi: 10.1177/87552930211030298

Wells, D. L., & Coppersmith, K. J. (1994). New empirical relationships among magnitude, rupture length, rupture width, rupture area, and surface displacement. *Bulletin of the Seismological Society of America*, *84*(4), 974-1002. doi: 10.1785/BSSA0840040974

Xu, S., Ben-Zion, Y., Ampuero, J.-P., & Lyakhovsky, V. (2015). Dynamic Ruptures on a Frictional Interface with Off-Fault Brittle Damage: Feedback Mechanisms and Effects on Slip and Near-Fault Motion. *Pure and Applied Geophysics*, *172*(5).

Yang, W., & Hauksson, E. (2013). The tectonic crustal stress field and style of faulting along the Pacific North America Plate boundary in Southern California. *Geophysical Journal International*, *194*.

Yeh, T., & Olsen, K. B. (2023). Fault Damage Zone Effects on Ground Motions during the 2019 Mw 7.1 Ridgecrest, California, Earthquake. *Bulletin of the Seismological Society of America*, *113*.

Zhou, Z., Bianco, M., Gerstoft, P., & Olsen, K. (2022). High-Resolution Imaging of Complex Shallow Fault Zones Along the July 2019 Ridgecrest Ruptures. *Geophysical Research Letters*, *49*.

Shallow fault zone structure affects rupture dynamics and ground motions of the 2019 Ridgecrest sequence to regional distances

Nico Schliwa[1], Alice-Agnes Gabriel[2,1], Yehuda Ben-Zion[3]

[1]Department of Earth and Environmental Sciences, Ludwig-Maximilians Universität München, Munich, Germany

[2]Scripps Institution of Oceanography, UC San Diego, La Jolla, USA

[3]Department of Earth Sciences and Statewide California Earthquake Center, University of Southern California, Los Angeles, USA

This document contains supplemental material to augment the main manuscript.

Contents of this file

1. Text S1 to S2
2. Figures S1 to S11
3. Tables S1

Additional Supporting Information (Files uploaded separately)

1. Captions for Movies S1 to S2

Text S1: Dynamic rupture simulation code

Dynamic rupture simulations are performed with the open-source software SeisSol (see Open research). SeisSol implements the arbitrary high-order accurate derivative discontinuous Galerkin (ADER-DG) method on unstructured tetrahedral elements (Dumbser & Käser, 2006; de la Puente et al., 2009), and is verified through numerous dynamic rupture benchmark problems (Pelties et al., 2014; Harris et al., 2018). SeisSol demonstrates high computational efficiency scaling up to full supercomputers using models with several billions degrees of freedom, achieving a significant fraction of the theoretical peak performance (Breuer et al., 2014; Uphoff et al., 2017; Krenz et al., 2021), and supports elastic, viscoelastic, viscoplastic, anisotropic, and poroelastic rheologies (Uphoff & Bader, 2016; Wollherr et al., 2018; Wolf et al., 2020, 2022).

Text S2: Computational mesh and model resolution

The fault zone and reference model share the same computational mesh (Taufiqurrahman et al., 2023). The mesh comprises 27.2 million elements and spans a domain of 200 km × 200 km horizontally and 100 km vertically, utilizing the WGS84/UTM Mercator 11S projection. The spatially adaptive mesh resolution is set to an element edge length of 500 m at the free surface and 75 m near faults to resolve the fault zone geometry and rupture dynamics. High-resolution topography from the Shuttle Radar Topography Mission (Farr et al., 2007) is incorporated. The simulations employ high-order basis functions of polynomial order 4, leading to a fifth-order space-time accurate numerical scheme. The chosen discretization resolves the wavefield up to at least 2 Hz in the near-source region and at least 1 Hz in our study region expanding to distances up to 140 km away from the Ridgecrest fault system. Fig. S3 and S4 show the synthetic and observed frequency content of five near-source stations.

Movie S1: Fault zone model mainshock ruture

Two perspectives on the slip rate evolution of the fault zone Ridgecrest mainshock dynamic rupture model: https://drive.google.com/file/d/1aGY8Hnc_sli6_aGj-FL_IGEEtZhREGpN/view?usp=sharing

Movie S2: Fault zone model foreshock and mainshock ruptures with surface ground motions

Accumulated slip evolution and surface ground motions of the foreshock and mainshock of the Ridgecrest sequence dynamic rupture models, including the fault zone. The movie displays two perspectives. https://drive.google.com/file/d/1VMtliDMPHQjw_2JfT3TO-QPjwxBygQHu/view?usp=sharing

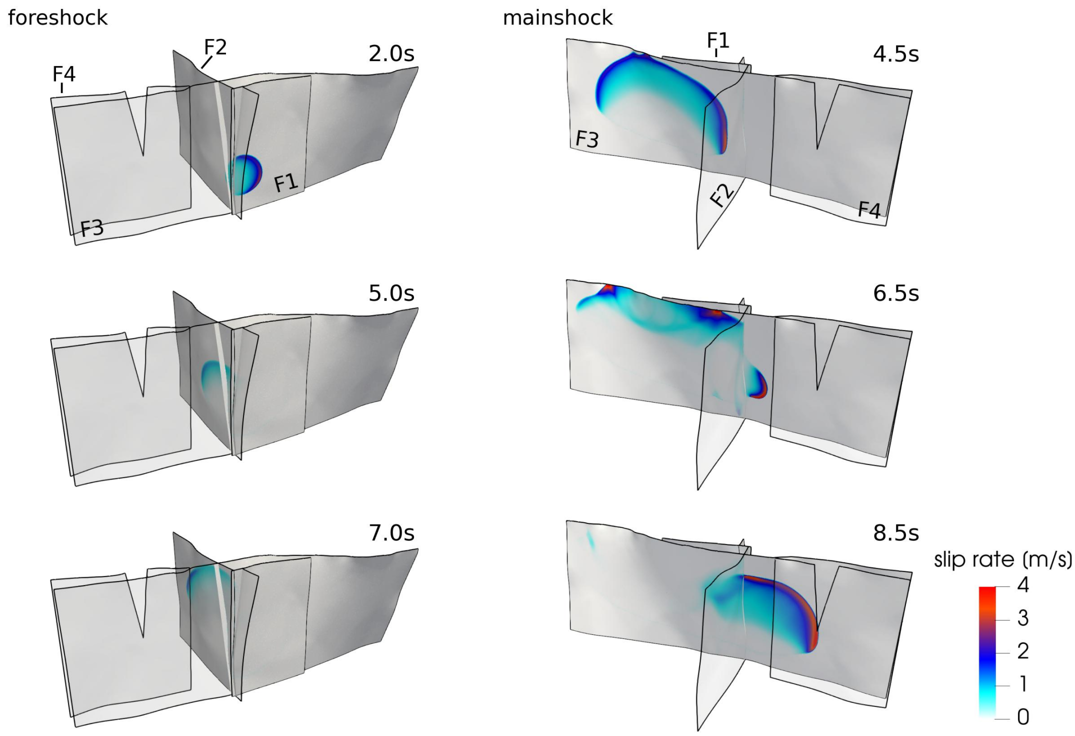

Figure S1. Slip rate snapshots of the Searles Valley foreshock and Ridgecrest mainshock dynamic rupture reference models (Taufiqurrahman et al., 2023) adapted from Fig. 3c in Schliwa and Gabriel (2023).

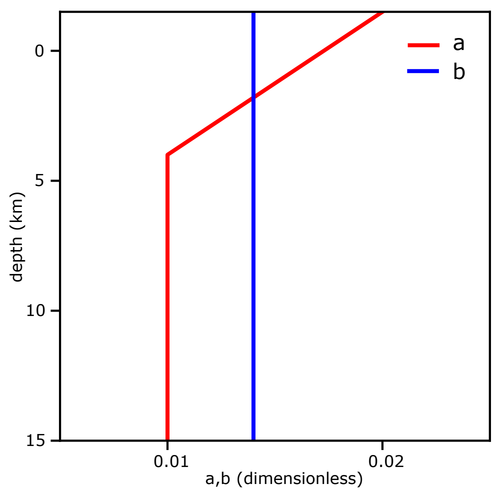

Figure S2. Depth profile of the a and b rate-and-state friction parameters (adapted from Figure S4 in Taufiqurrahman et al., 2023)

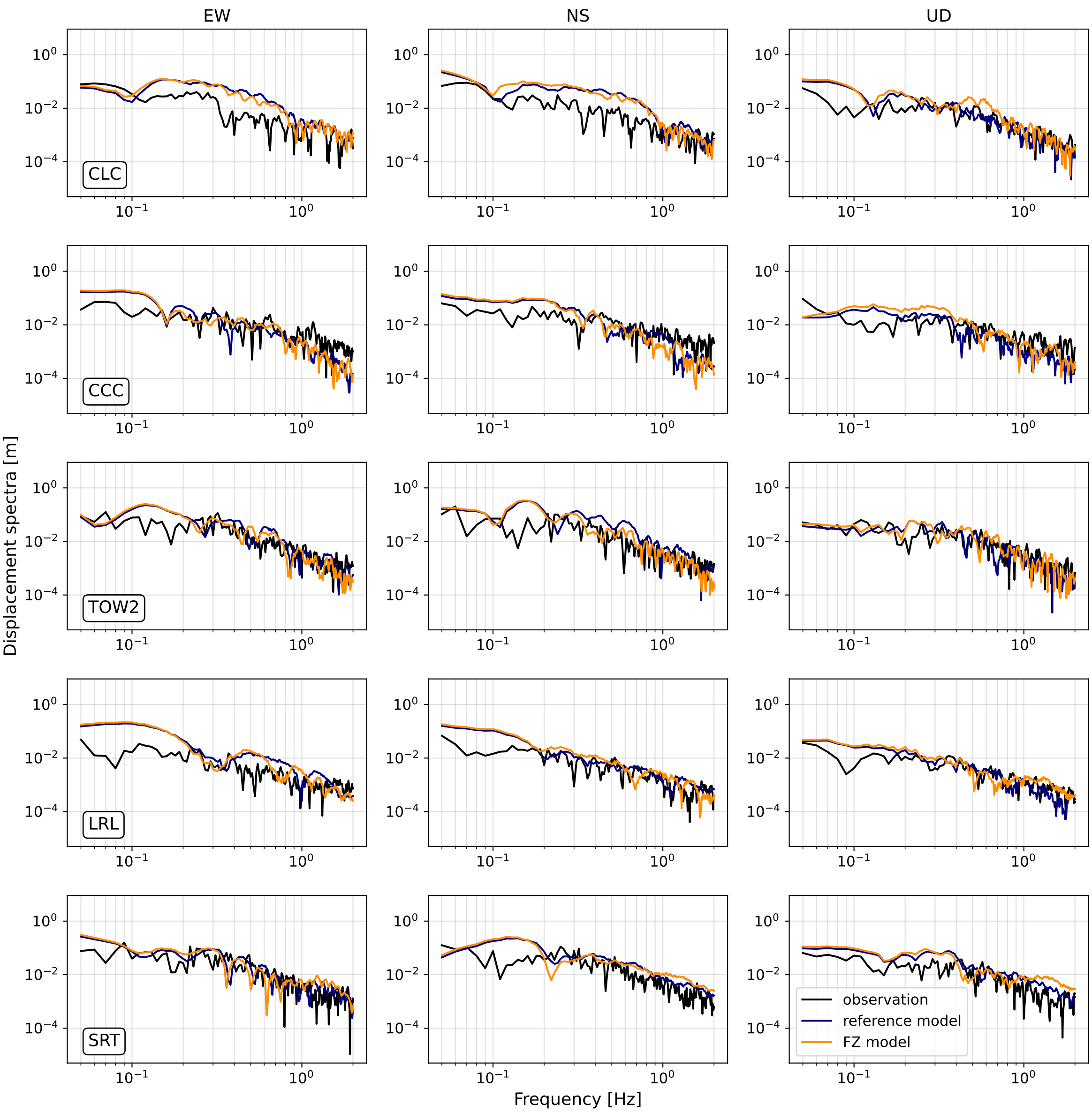

Figure S3. Comparison of the displacement spectra of the reference and FZ Searles Valley foreshock dynamic rupture models with observations from five near-source stations. Spectra are not normalized and represent physical units. The text boxes indicate the respective station codes. Station locations are shown in Fig. 1.

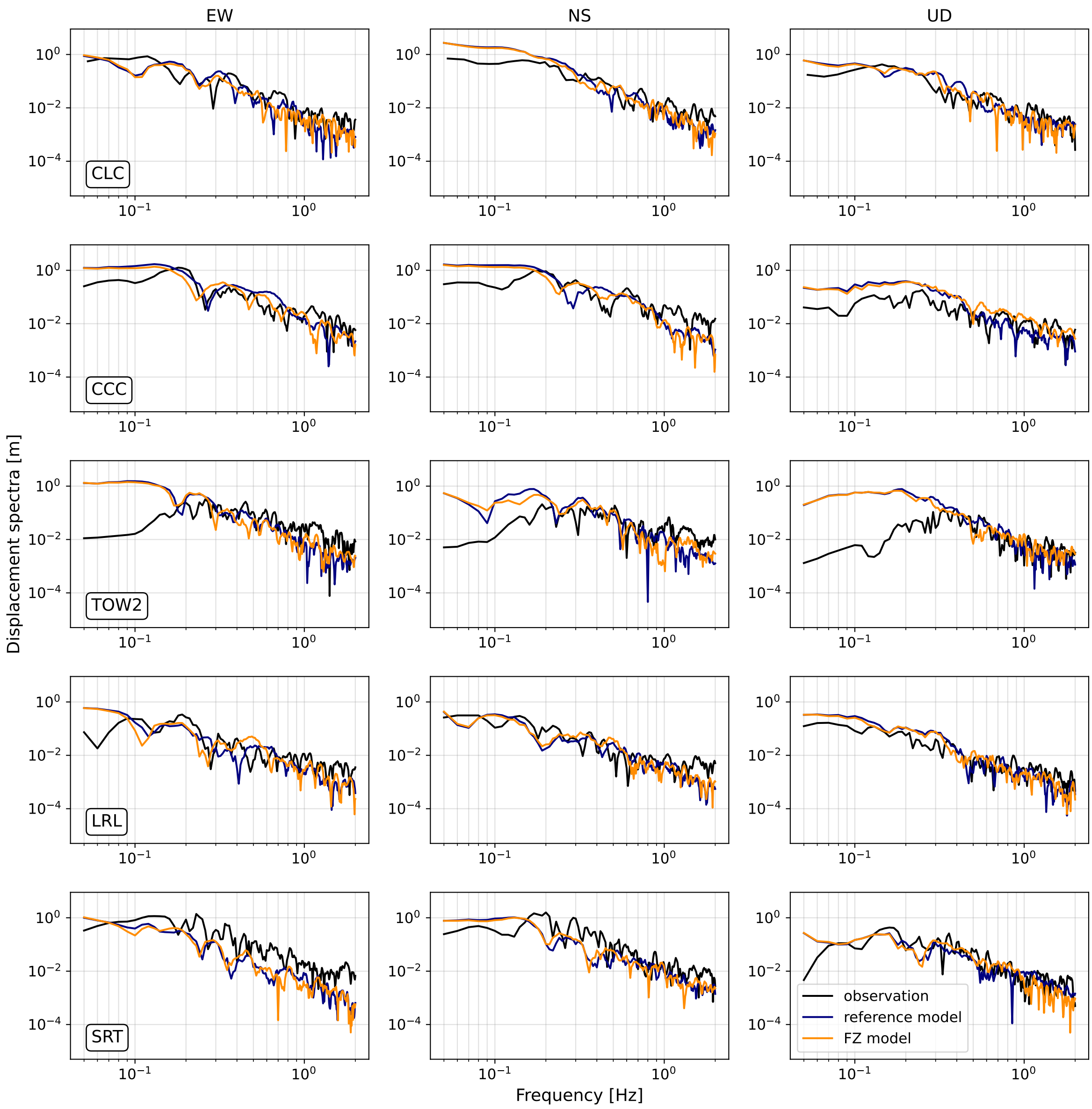

Figure S4. Comparison of the displacement spectra of the reference and FZ Ridgecrest mainshock dynamic rupture models with observations from five near-source stations. Spectra are not normalized and represent physical units. The text boxes indicate the respective station codes. Station locations are shown in Fig. 1.

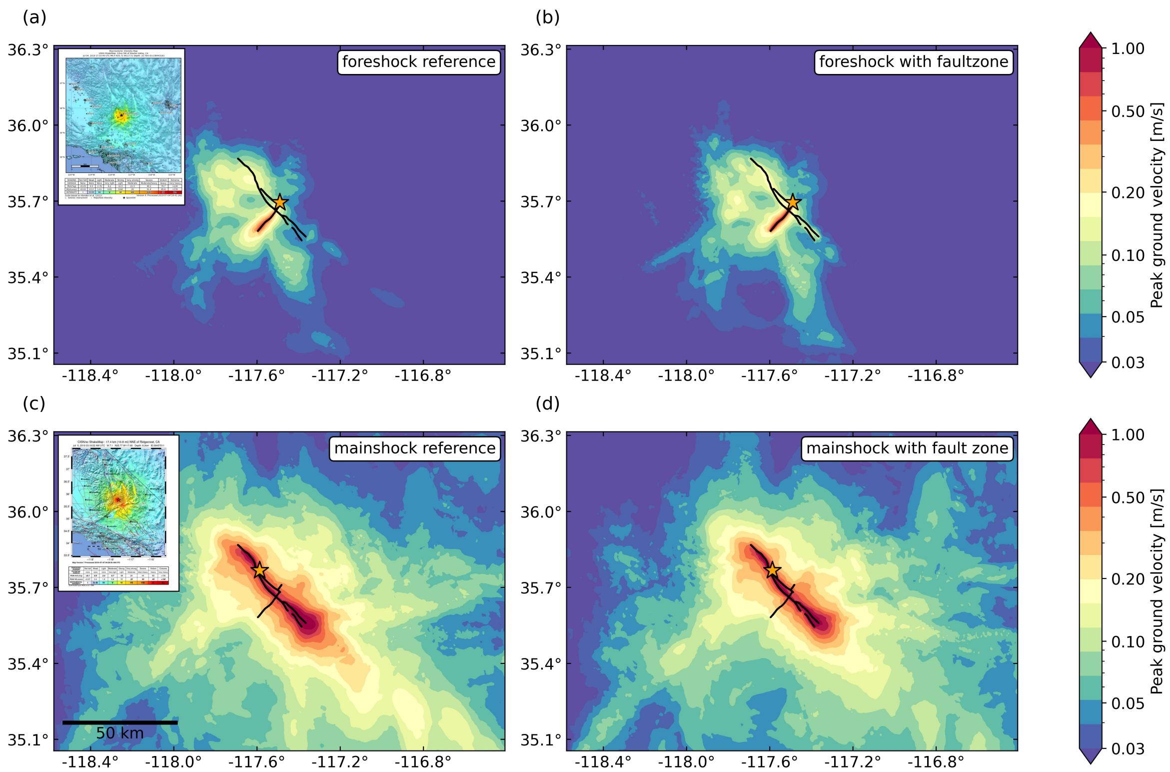

Figure S5. Regional peak ground velocity distribution of the (a) Searles Valley foreshock reference dynamic rupture model. (b) Searles Valley foreshock dynamic rupture FZ model. (c) Ridgecrest mainshock reference dynamic rupture model. (d) Ridgecrest mainshock dynamic rupture FZ model. The shown peak ground velocities represent rotationally independent geometric means (GMRotD50, Boore et al., 2006). Insets show USGS intensity shakemaps (Wald et al., 2022) of the corresponding events.

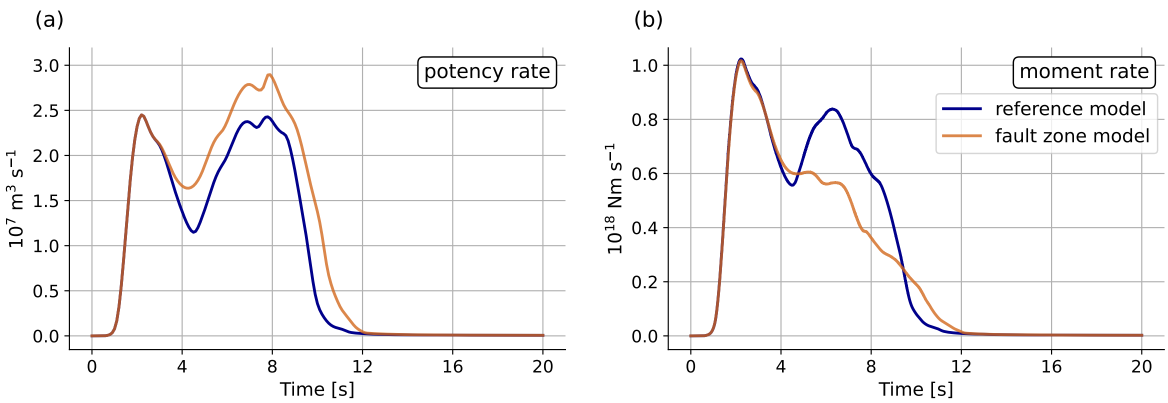

Figure S6. (a) Potency and (b) moment release rates of the Searles Valley foreshock dynamic rupture models with and without a fault damage zone.

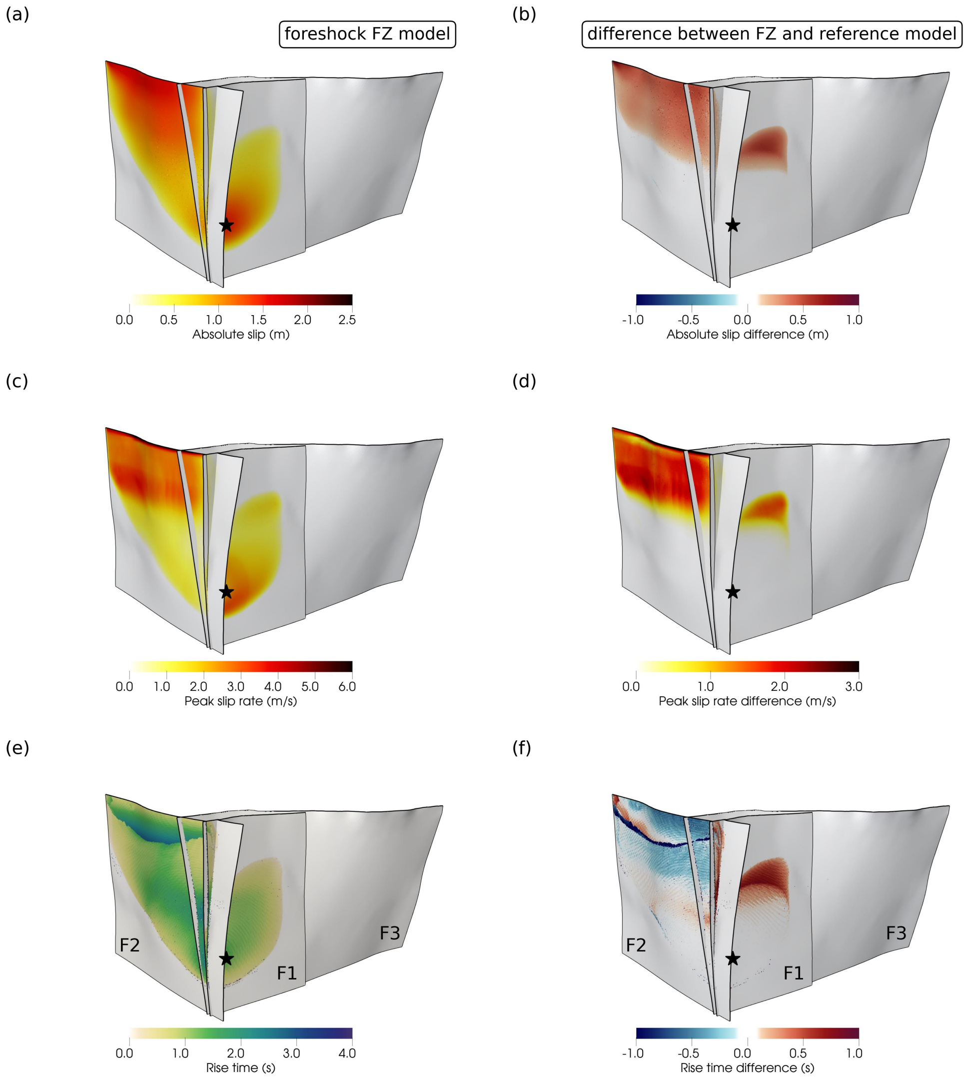

Figure S7. Dynamic rupture parameters of the Searles Valley foreshock FZ model and the differences to the reference model: (a) Absolute slip. (b) Absolute slip difference. (c) Peak slip rate. (d) Peak slip rate difference. (e) Rise time. (f) Rise time difference. The southern part of the fault system is cut out to improve visibility of the foreshock rupture.

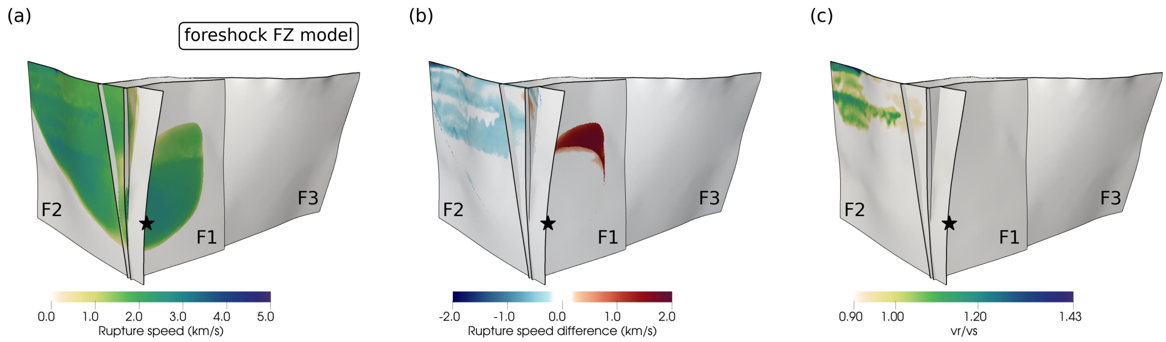

Figure S8. (a) Rupture speed distribution of the Searles Valley foreshock FZ model. (b) Rupture speed difference between the FZ and reference model of the Searles Valley foreshock. (c) Ratio between rupture speed and local S-wave velocity (v_r/v_s) of the FZ foreshock model. The colorbar is saturated to highlight supershear rupture. The southern part of the fault system is cut out to improve visibility of the foreshock rupture.

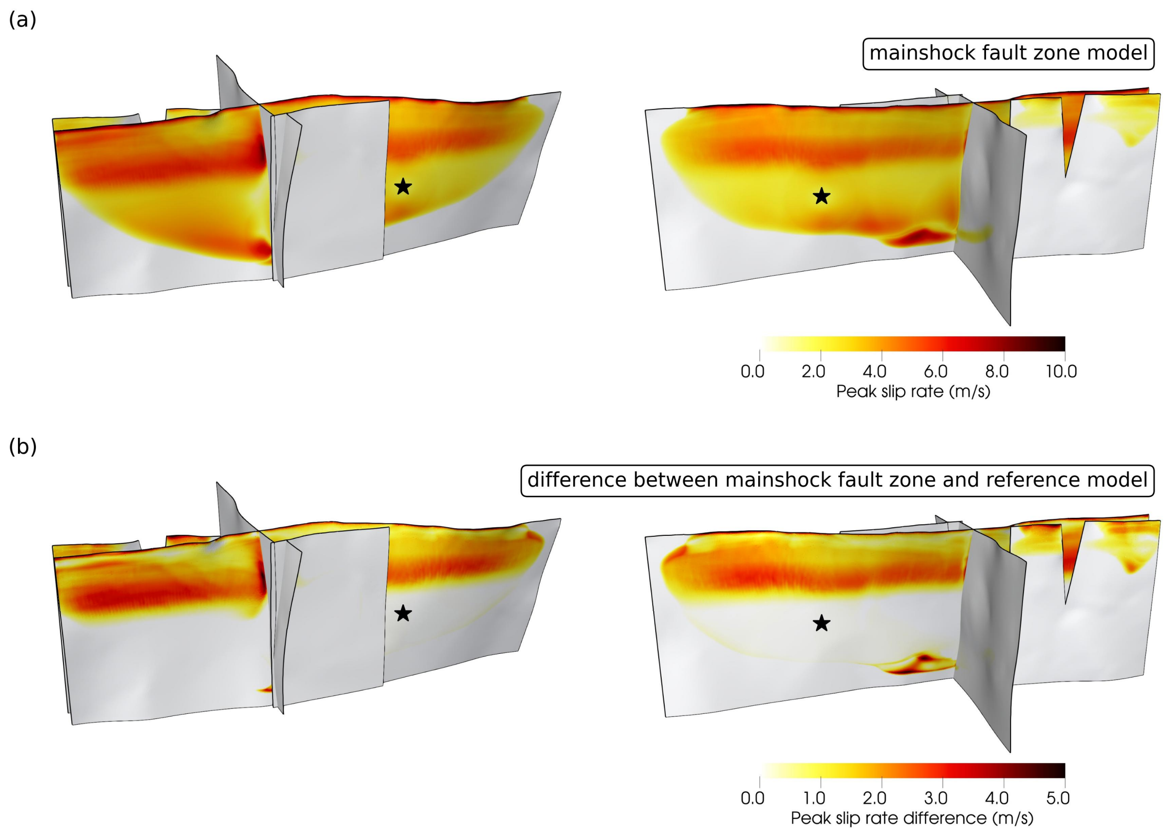

Figure S9. (a) Two perspectives of the fault zone model's peak slip rate distribution of the Ridgecrest mainshock. (b) Two perspectives of the peak slip rate difference ($\mathrm{PSR}_{fz} - \mathrm{PSR}_{ref}$) between the fault zone model and the reference model of the Ridgecrest mainshock.

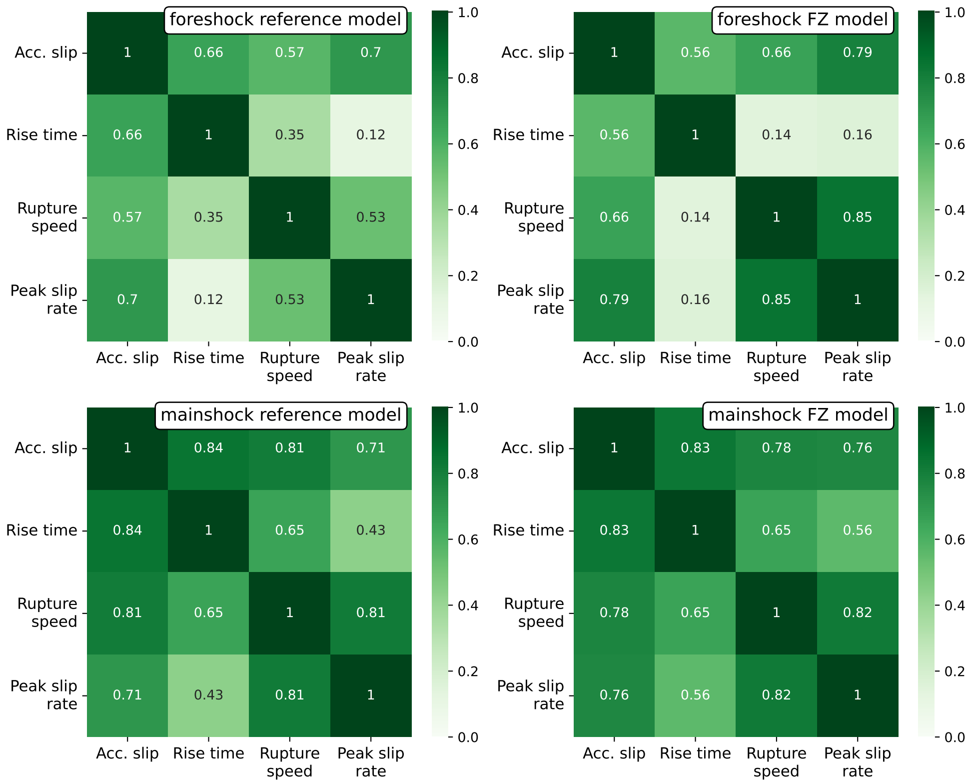

Figure S10. Spatial correlation matrices of kinematic rupture parameters of the different dynamic rupture models of the 2019 Ridgecrest sequence, following (Schmedes et al., 2010). Correlation coefficients are computed from fault elements where the accumulated slip exceeds 0.01 m. We normalize the rupture speed by the fault-local S-wave velocity. Rise time is defined by the period the absolute slip rate exceeds 0.1 m/s.

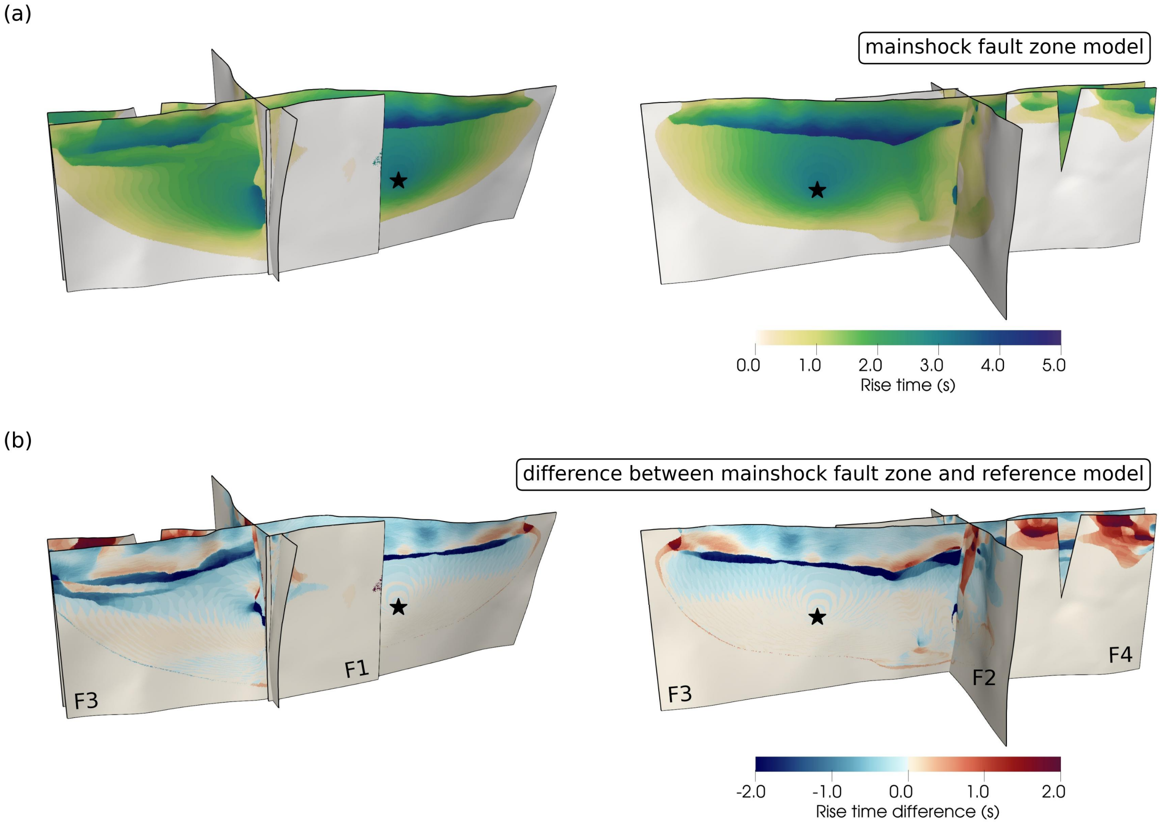

Figure S11. (a) Two perspectives of the rise time distribution of the Ridgecrest mainshock dynamic rupture model, including the fault damage zone. Rise time is defined by the period the absolute slip rate exceeds 0.1 m/s. (b) Two perspectives of the rise time difference $(t_{r,fz} - t_{r,ref})$ between the fault damage zone model and the reference model of the Ridgecrest mainshock.

Table S1. Fast velocity-weakening rate-and-state friction parameters of the 2019 Ridgecrest sequence dynamic rupture models (Table S2 in Taufiqurrahman et al., 2023).

Parameter	**Symbol**	**Value**
Direct-effect parameter	a	0.01-0.02
Evolution-effect parameter	b	0.014
Reference slip rate	V_0	10^{-6} m/s
Steady-state low-velocity friction coefficient at the slip rate V_0	f_0	0.6
Characteristic slip distance of the state evolution	L	0.2
Full weakened friction coefficient	f_{w}	0.1
Initial slip rate	V_{ini}	10^{-16} m/s
Weakened slip rate	V_{w}	0.1 m/s

References

Boore, D. M., Watson-Lamprey, J., & Abrahamson, N. A. (2006). Orientation-Independent Measures of Ground Motion. *Bulletin of the Seismological Society of America*, *96*.

Breuer, A., Heinecke, A., Rettenberger, S., Bader, M., Gabriel, A.-A., & Pelties, C. (2014). Sustained Petascale Performance of Seismic Simulations with SeisSol on SuperMUC. In *Proceedings of the international supercomputing conference* (pp. 1–18). Cham: Springer International Publishing.

de la Puente, J., Ampuero, J.-P., & Käser, M. (2009). Dynamic rupture modeling on unstructured meshes using a discontinuous Galerkin method. *Journal of Geophysical Research: Solid Earth*, *114*.

Dumbser, M., & Käser, M. (2006). An arbitrary high-order discontinuous Galerkin method for elastic waves on unstructured meshes — II. The three-dimensional isotropic case. *Geophysical Journal International*, *167*(1). doi: 10.1111/j.1365-246X.2006.03120.x

Farr, T. G., Rosen, P. A., Caro, E., Crippen, R., Duren, R., Hensley, S., … Alsdorf, D. (2007). The Shuttle Radar Topography Mission. *Reviews of Geophysics*, *45*(2).

Harris, R. A., Barall, M., Aagaard, B., Ma, S., Roten, D., Olsen, K., … Dalguer, L. (2018). A Suite of Exercises for Verifying Dynamic Earthquake Rupture Codes. *Seismological Research Letters*, *89*.

Krenz, L., Uphoff, C., Ulrich, T., Gabriel, A.-A., Abrahams, L. S., Dunham, E. M., & Bader, M. (2021). 3D Acoustic-Elastic Coupling with Gravity: The Dynamics of the 2018 Palu, Sulawesi Earthquake and Tsunami. In *The International Conference for High Performance Computing, Networking, Storage and Analysis.* Association for Computing Machinery. doi: 10.1145/3458817.3476173

Pelties, C., Gabriel, A.-A., & Ampuero, J.-P. (2014). Verification of an ADER-DG method for complex dynamic rupture problems. *Geoscientific Model Development*, *7*.

Schliwa, N., & Gabriel, A. (2023). Equivalent Near-Field Corner Frequency Analysis of 3D Dynamic Rupture Simulations Reveals Dynamic Source Effects. *Seismological Research Letters*, *95*.

Schmedes, J., Archuleta, R. J., & Lavallée, D. (2010). Correlation of earthquake source parameters inferred from dynamic rupture simulations. *Journal of Geophysical Research: Solid Earth*, *115*(B3). doi: 10.1029/2009JB006689

Taufiqurrahman, T., Gabriel, A.-A., Li, D., Ulrich, T., Li, B., Carena, S., ... Gallovič, F. (2023). Dynamics, interactions and delays of the 2019 Ridgecrest rupture sequence. *Nature*. doi: 10.1038/s41586-023-05985-x

Uphoff, C., & Bader, M. (2016). Generating high performance matrix kernels for earthquake simulations with viscoelastic attenuation. In *Proceedings of the 2016 international conference on high performance computing and simulation* (p. 908-916).

Uphoff, C., Rettenberger, S., Bader, M., Madden, E. H., Ulrich, T., Wollherr, S., & Gabriel, A.-A. (2017). Extreme scale multi-physics simulations of the tsunamigenic 2004 sumatra megathrust earthquake. In *Proceedings of the international conference for high performance computing, networking, storage and analysis* (p. 21).

Wald, D. J., Worden, C. B., Thompson, E. M., & Hearne, M. (2022). ShakeMap operations, policies, and procedures. *Earthquake Spectra*, *38*(1), 756-777. doi: 10.1177/87552930211030298

Wolf, S., Gabriel, A.-A., & Bader, M. (2020). Optimization and Local Time Stepping of an ADER-DG Scheme for Fully Anisotropic Wave Propagation in Complex Geometries. In *Computational Science – ICCS 2020* (pp. 32–45). Cham: Springer International Publishing. doi: 10.1007/978-3-030-50420-5_3

Wolf, S., Galis, M., Uphoff, C., Gabriel, A.-A., Moczo, P., Gregor, D., & Bader, M. (2022). An efficient ADER-DG local time stepping scheme for 3D HPC simulation of seismic waves in poroelastic media. *Journal of Computational Physics*, *455*.

Wollherr, S., Gabriel, A.-A., & Uphoff, C. (2018). Off-fault plasticity in three-dimensional dynamic rupture simulations using a modal Discontinuous Galerkin method on unstructured meshes: implementation, verification and application. *Geophysical Journal International*, *214*(3). doi: 10.1093/gji/ggy213